Department of Engineering Physics and Mathematics
Laboratory of Biomedical Engineering
Helsinki University of Technology
Espoo, Finland

Cardiomagnetic Source Imaging

Katja Pesola

Dissertation for the degree of Doctor of Science in Technology to be presented with due permission for public examination and debate in Auditorium F1 at Helsinki University of Technology (Espoo, Finland) on the 19th of May, 2000, at 12 o'clock noon.

Espoo 2000

ISBN 951–22–4962–6
Printing house Picaset, Helsinki 2000

Contents

List of publications

This thesis consists of an overview and of the following eight publications:

I K. Pesola, U. Tenner, J. Nenonen, P. Endt, H. Brauer, U. Leder, and T. Katila: Multichannel magnetocardiographic measurements with a physical thorax phantom. *Medical & Biological Engineering & Computing* **37**, pp. 2–7, 1999.

II R. Fenici, J. Nenonen, K. Pesola, P. Korhonen, J. Lötjönen, M. Mäkijärvi, L. Toivonen, V–P. Poutanen, P. Keto, and T. Katila: Nonfluoroscopic localisation of an amagnetic stimulation catheter by multichannel magnetocardiography. *Pacing and Clinical Electrophysiology* **22**, pp. 1210–1220, 1999.

III K. Pesola, J. Nenonen, R. Fenici, J. Lötjönen, M. Mäkijärvi, P. Fenici, P. Korhonen, K. Lauerma, M. Valkonen, L. Toivonen, and T. Katila: Bioelectromagnetic localization of a pacing catheter in the heart. *Physics in Medicine and Biology* **44**, pp. 2565–2578, 1999.

IV K. Pesola, J. Lötjönen, J. Nenonen, I.E. Magnin, K. Lauerma, R. Fenici, and T. Katila: The effect of geometric and topologic differences in boundary element models on magnetocardiographic localization accuracy. Accepted for publication in *IEEE Transactions on Biomedical Engineering*, 2000.

V K. Pesola, J. Nenonen, R. Fenici, and T. Katila: Comparison of regularization methods when applied to epicardial minimum norm estimates. *Biomedizinische Technik* **42** (Suppl. 1), pp. 273–276, 1997.

VI K. Pesola, H. Hänninen, K. Lauerma, J. Lötjönen, M. Mäkijärvi, J. Nenonen, P. Takala, L.–M. Voipio–Pulkki, L. Toivonen, and T. Katila: Current density estimation on the left ventricular epicardium: A potential method for ischemia localization. *Biomedizinische Technik* **44** (Suppl. 2), pp. 143–146, 1999.

VII T. Oostendorp and K. Pesola: Non–invasive determination of the activation sequence of the heart: Validation by comparison with invasive human data. *In* A. Murray and S. Swiryn (Eds.): *Computers in Cardiology* **25**, pp. 313–316, 1998.

VIII K. Pesola, T. Oostendorp, J. Nenonen, P. Korhonen, J. Lötjönen, L. Toivonen, and T. Katila: Uniform double layer solutions for magnetocardiographic and body surface potential mapping data. *In* T. Yoshimoto, M. Kotani, S. Kuriki, H. Karibe and N. Nakasato (Eds.): *Recent Advances in Biomagnetism: Proceedings of the 11th International Conference on Biomagnetism*, Tohoku University Press, Sendai, pp. 290–293, 1999.

Summary of publications

The eight publications included in this thesis are the result of team work carried out at the Laboratory of Biomedical Engineering between the technical experts, medical collaborators from the Helsinki University Central Hospital and foreign researchers in the field of electro– and magnetocardiography. The author has actively taken part in the research work presented in the publications. In the following, a brief summary of each publication and the statement of the author's involvement will be provided.

I: Multichannel magnetocardiographic measurements with a physical thorax phantom (*Medical & Biological Engineering & Computing* **37**, pp. 2–7, 1999)
In this work, a novel non–magnetic thorax phantom and artificial dipolar sources were applied in assessing the accuracy of magnetocardiographic (MCG) equivalent current dipole (ECD) localizations. The data were recorded in the same clinical environment where the patient studies are carried out. The localizations were found to be accurate within a few millimeters, provided that the signal–to–noise ratio (SNR) and the goodness of fit of the localizations were sufficiently high. The dependence of the goodness of fit on the SNR was derived, and the experimental results were found to correspond to the derived model. The ECD localization accuracies obtained in this study, evaluated in certain ranges of the SNR and of the goodness of fit, are an indication of the best possible accuracy achievable in clinical studies.

II: Nonfluoroscopic localization of an amagnetic stimulation catheter by multichannel magnetocardiography (*Pacing and Clinical Electrophysiology* **22**, pp. 1210–1220, 1999)
The accuracy of magnetocardiographic ECD localizations was investigated in five patients using a non–magnetic stimulation catheter. The position of the tip of the catheter was documented on biplane cine X–ray images. MCG signals were then recorded during cardiac pacing. Non–invasive localizations of the tip of the catheter were computed using individual, homogeneous boundary element models to model the torso. The mean distance between the tip of the catheter determined from fluoroscopy and MCG localizations was 11 $\pm$ 4 mm. The mean distance between the localizations calculated during the stimulus spikes and in the beginning of the evoked responses was 4 $\pm$ 1 mm. The accurate 3D localizations of the tip of the catheter suggest that the MCG method could be developed towards a useful clinical tool during electrophysiological studies.

III: Bioelectromagnetic localization of a pacing catheter in the heart (*Physics in Medicine and Biology* **44**, pp. 2565–2578, 1999)

In this work, the non–magnetic catheter was applied in 10 patients. Biplane fluoroscopic imaging with lead ball markers was again used to record the catheter position. In addition to the MCG recordings, simultaneous multichannel body surface potential mapping (BSPM) recordings were performed at the BioMag Laboratory during catheter pacing. ECD localizations were computed from MCG and BSPM data, employing standard and patient–specific boundary element torso models. Using individual models with the lungs included, the average MCG localization error was 7 ± 3 mm, whereas the average BSPM localization error was 25 ± 4 mm. The results of this study indicate that the accuracy of ECD localizations calculated from MCG data is superior to the accuracy obtainable from BSPM measurements.

IV: The effect of geometric and topologic differences in boundary element models on magnetocardiographic localization accuracy (Accepted for publication in *IEEE Transactions on Biomedical Engineering*, 2000)

The study was performed to evaluate the changes in MCG dipole localization results when the geometry and the topology of the torso model were altered. Three reference torso models were manipulated to mimic various sources of error in the measurement and analysis procedures. The effect of each modification was investigated by calculating 3D distances from the "gold standard" ECD localizations, obtained with the reference models, to the locations obtained with the modified models. The effect of inhomogeneities (lungs, intra–ventricular blood) was found to be significant for deep source locations. However, superficial sources could be localized within a few millimeters even with non–individual torso models. In general, the thorax model should extend long enough in the pelvic region, and the positions of the lungs and the ventricles should be known in order to obtain accurate localizations.

V: Comparison of regularization methods when applied to epicardial minimum norm estimates (*Biomedizinische Technik* **42** (Suppl. 1), pp. 273–276, 1997)

In this study, MCG measurements of five patients with the non–magnetic catheter in the heart were used to validate the calculated minimum norm, or current density, estimates. The estimates were computed at the stimulus spikes and during the following depolarization on the triangulated epicardial surfaces using different regularization techniques. The applied techniques were: (i) the truncation of the singular value decomposition, (ii) Tikhonov regularization, (iii) weighting and (iv) recursive weighting. When the Tikhonov method was used, the value of the regularization parameter was determined by means of the L–curve. In techniques (iii) and (iv), the square roots of

the optimal dipole amplitudes were applied. The results of the study showed that when the source was located within 8 cm from the sensors, all regularization techniques were able to localize the center point of the source current distribution correctly. However, the estimates calculated for a relatively deep source (13 cm away from the sensors) clearly showed the need for weighting. In this case, the techniques (i) and (ii) failed to give a meaningful description about the underlying activity.

VI: Current density estimation on the left ventricular epicardium: A potential method for ischemia localization (*Biomedizinische Technik* **44** (Suppl. 2), pp. 143–146, 1999)

Different regularization operators applicable in Tikhonov regularization were tested by calculating current density estimates (CDEs) from simulated MCG data on the epicardial surface of the left ventricle. Second–order regularization was found to be superior to zero–order regularization. In addition to simulations, CDE was applied in 13 coronary artery disease (CAD) patients. MCG measurements were performed at rest and after stress using a non–magnetic exercise ergometer. CDEs were calculated from the ST–segment difference signals. In four single–vessel CAD patients, an increase in the CDE amplitude was found to correlate with the expected ischemic myocardial region. In nine three–vessel CAD patients, PET was used as a reference in separating the areas of viable myocardial tissue from scar regions. In this patient group, the areas of low CDE amplitude were found to match with scar regions whereas a high CDE amplitude was found to correlate with viable areas.

VII: Non–invasive determination of the activation sequence of the heart: Validation by comparison with invasive human data (*In:* A. Murray, S. Swiryn (Eds.): *Computers in Cardiology* **25**, pp. 313–316, 1998)

In this paper, results from a validation study carried out with the uniform double layer (UDL) source model were presented. Invasive human data obtained from four patients with an old myocardial infarction that underwent open–chest surgery in order to treat ventricular arrhythmia were used in the validation. During surgery, the epicardial activation was mapped by using an electrode sock wrapped around the heart. The invasively determined activation maps were compared to the calculated activation times, obtained from BSPM data measured prior to surgery. The overall patterns (such as breakthroughs and regions of late activation) were reproduced quite well in the computed data sets. However, there was a clear difference in the precise locations of these sites. This could be caused by the uncertainty in the positions of the epicardial electrodes, or by the infarcted regions for which the assumption about a uniform double layer does not hold.

VIII: Uniform double layer solutions for magnetocardiographic and body surface potential mapping data (*In:* T. Yoshimoto, M. Kotani, S. Kuriki, H. Karibe and N. Nakasato (Eds.): *Recent Advances in Biomagnetism: Proceedings of the 11th International Conference on Biomagnetism*, Tohoku University Press, Sendai, pp. 290–293, 1999)

In this study, the properties and the accuracy of the ventricular activation times, calculated from MCG data, were compared to those of invasive and BSPM data presented in Publication VII. The qualitative comparison between the measured and the calculated epicardial activation times showed that the calculated maps were, in general, in good agreement with the measured data. However, certain differences were present both in the MCG and BSPM maps. In the quantitative comparison, the activation times at the electrode locations, calculated from MCG data, had an average relative difference of 29 % with respect to the measured data while for BSPM maps the average relative difference was found to be 37 %. However, more accurate information about the locations of the invasive electrodes would be necessary to make a reliable quantitative comparison.

Statement of involvement

In Publication I, the author performed the magnetic measurements with the physical thorax phantom together with Dr. Uwe Tenner and carried out the analysis of the measurements. Publication I was also written by the author. Publications II and III are the result of a co–operation with Prof. Riccardo Fenici from the Catholic University of Rome, Italy. In Publication II, the author was mainly responsible for performing the MCG recordings at the BioMag Laboratory as well as participated actively in computing the ECD localizations and analyzing the X–ray results. In Publication III, the author was responsible for carrying out the simultaneous MCG and BSPM recordings and a large share of the analysis of the data. Publication III was also written by the author. In Publication IV, the ECD calculations were performed by the author, and it was written in co–operation with Dr. Jyrki Lötjönen. The calculation of the current density estimates in Publications V and VI was implemented and performed by the author. The publications were also written by her. Publications VII and VIII are the result of a collaboration with Dr. Thom Oostendorp from the University of Nijmegen, the Netherlands. The author has performed most of the inverse calculations from MCG and BSPM data, as well as written Publication VIII.

List of abbreviations

The most important abbreviations used in the overview are listed and explained below.

AT	activation time
AV	atrio–ventricular
BE	boundary element
BEM	boundary element method
BSPM	body surface potential mapping
CAD	coronary artery disease
CDE	current density estimate
CEF	cardiac evoked field
CEP	cardiac evoked potential
DC	direct current
ECD	equivalent current dipole
ECG	electrocardiography
EP	electrophysiological
FEM	finite element method
gSVD	generalized singular value decomposition
HT_C	high–temperature
HUCH	Helsinki University Central Hospital
HUT	Helsinki University of Technology
LAD	left anterior descending coronary artery
LCX	left circumflex coronary artery
LT_C	low–temperature
LV	left ventricle
LVH	left ventricular hypertrophy
MCG	magnetocardiography
MI	myocardial infarction
MNE	minimum norm estimate
MR	magnetic resonance
MRI	magnetic resonance imaging
PET	positron emission tomography
RCA	right coronary artery
RF	radio–frequency
RMS	root–mean–square
RV	right ventricle
SA	sino–atrial
SNR	signal–to–noise ratio
SQUID	superconducting quantum interference device
SVD	singular value decomposition
tSVD	truncated singular value decomposition
UDL	uniform double layer
VT	ventricular tachycardia
WPW	Wolff–Parkinson–White

List of symbols

The most important symbols of the overview are listed and shortly explained below. Vectors and vector functions are denoted with boldface letters.

$\mathbf{J_i}$	(microscopic) impressed current density [A/m^2]
$\mathbf{J_p}$	(macroscopic) primary current density [A/m^2]
$\mathbf{J_v}$	volume current density [A/m^2]
$\mathbf{J_{tot}}$	total (quasi–static) current density [A/m^2]
$\mathbf{E}$	electric field [V/m]
$\mathbf{B}$	magnetic flux density [T] (in this thesis referred to as the magnetic field)
∇	gradient operator (nabla)
ρ	total charge density [C/m^3]
ϵ_0	electric permittivity in vacuum [F/m]
μ_0	magnetic permeability in vacuum [H/m]
σ	electric conductivity [S/m]
ϕ	electric potential [V]
$\mathbf{r}$	position vector referring to an observation (field) point
$\mathbf{r}\,'$	position vector referring to an integration (source) point
V'	a bounded volume conductor containing the current sources
S_k	bounding surface in a piecewise homogeneous torso model
M	number of surfaces in a piecewise homogeneous torso model
$h_i(\cdot)$	basis function in boundary element formulation
Δ_i	flat triangular boundary element
Ω	solid angle matrix
I	identity matrix
g	goodness of fit
m	number of sensors
n	number of source points
$\mathbf{L}_i$	magnetic lead field vector of the i^{th} sensor
L	lead field matrix
Γ	inner product matrix of the lead fields
$\mathbf{J}^*$	minimum norm estimate
$\mathbf{J}$	current density estimate
λ	regularization parameter
R	regularization operator
$D2$	discrete approximation of the surface Laplacian
μ_i	generalized singular value
κ	curvature function
D	weighting (or pre–conditioning) matrix
F	magnetic field component or electric potential in the UDL formulation
$A(\cdot,\cdot)$	magnetic or electric transfer function in the UDL formulation
$H(\cdot)$	Heaviside step function
τ	activation time on the ventricular surface [s]

1 Introduction

The electric current related to the functioning of the human heart causes differences in the electric potential inside the body. The measurement of these potential differences on the body surface, known as *electrocardiography* (ECG), was developed as a clinical tool already in the beginning of the 20th century. By now, the ECG has established an important role in clinical diagnosis and research of the cardiac function (e.g., MacFarlane and Lawrie 1988). In a more recent approach, ECG signals are collected with an electrode array to achieve denser spatial sampling. Measuring ECGs this way is usually referred to as *body surface potential mapping* (BSPM) since the anterior and posterior surfaces of the upper body (the torso) are covered with electrodes.

The same current sources in the heart generating the ECG also give rise to a magnetic field inside and outside of the body. The magnetic field produced by the heart was first measured by Baule and McFee (1963). This result gave birth to *magnetocardiography* (MCG) (e.g., Siltanen 1988). The maximum amplitude of the magnetic field generated by the human heart, approximately 10^{-10} T, is several orders of amplitude weaker than the earth's magnetic field. Therefore, the detection of MCG requires sensitive detectors and usually also shielding against external magnetic disturbances. Nowadays, the detection of MCG is based on highly sensitive sensors, Superconducting QUantum Interference Devices (SQUIDs), which were invented in the 1960's. In an MCG measurement, the sensors are usually arranged in a plane or in a concave surface close to the chest of the patient. The measurement is completely *non–invasive*, i.e. no contact, external media, electromagnetic fields or other radiation are directed towards the subject to be measured. As with ECG signals, information about the function of the heart is obtained with millisecond time resolution.

Estimating the bioelectric current sources in the body from biomagnetic measurements is often referred to as magnetic source imaging or functional source localization (e.g., Hämäläinen and Nenonen 1999). Therefore, the corresponding estimation in the heart is called *cardiomagnetic source imaging*. With a high enough localization accuracy of the current sources in the heart, valuable information can be provided, e.g., for the pre–ablative evaluation of arrhythmia patients. This evaluation is of special importance since nowadays the radio–frequency (RF) catheter ablation has replaced antiarrhythmic drug therapy for the treatment of many types of cardiac arrhythmias (Morady 1999). For example, in the Wolff–Parkinson–White (WPW) patient group with an accessory conducting pathway from the atria into the ventricles, RF ablation has eliminated the need for surgical ablation in almost all patients and the need for antiarrhythmic–drug therapy in many patients. The efficacy of catheter ablation depends on the accurate identification of the site of the origin of arrhythmia. Successful MCG results have been reported in locating the abnormal ventricular pre–excitation sites associated with the WPW–syndrome, origin of ventricular

extrasystolic beats, and origin of atrial arrhytmias (e.g., Nenonen *et al* 1991a, Ribeiro *et al* 1992, Weismüller *et al* 1992, Fenici and Melillo 1993, Mäkijärvi *et al* 1993, Oeff and Burghoff 1994, Moshage *et al* 1996). A prolonged exposure to radiation can therefore be reduced by taking into account the MCG localization result in the ablation procedure. Furthermore, preliminary studies also carried out in this thesis indicate that ischemic areas, i.e. areas which are suffering from lack of oxygen, and infarcted regions could be localized from multichannel MCG recordings. In addition to localization studies, multichannel MCG and BSPM studies have shown to be especially promising in evaluating the risk of life–threatening arrhythmias in different cardiac pathologies, especially after myocardial infarction (e.g., Montonen *et al* 1995, Hubley–Kozey *et al* 1995). A recent review on MCG and BSPM studies has been presented by Stroink *et al* (1996), and on magnetic source imaging in the brain and in the heart by Hämäläinen and Nenonen (1999).

In source localization studies, the *forward problem* has to be solved first, i.e. one has to calculate the electric potential or the magnetic field, generated by the current sources in the heart, on and outside of the body, respectively. In the *inverse problem*, the current source is determined from the MCG and/or BSPM measurements. However, even with a complete knowledge of the electromagnetic field outside of the source region, the inverse problem cannot be uniquely solved because the same field distribution can be produced by infinitely many current source configurations. Therefore, restrictive assumptions about the current sources are needed. The conventional way is to use equivalent *source models* for describing the actual currents. The parameters of the source model can then be determined from the measured data, e.g., in a least–squares sense. In addition to the current source, the media surrounding it needs to modeled. The volume conductor models used in cardiomagnetic source imaging studies are usually referred to as *torso models*.

In this thesis, the aim was to investigate the obtaible accuracy of cardiomagnetic source imaging results using different source models. In addition, the effect of the torso model on the localization accuracy was examined. In some studies, also body surface potential mapping data were used for comparison purposes. A high impact was given to clinical applications, i.e. how the calculation methods would work in patients. In Section 2, the basic theory related to modeling the torso and the current sources inside the heart is presented as background information. The most commonly used source model, the equivalent current dipole (ECD), and studies related to it are described in Section 3. The obtainable accuracy of ECD localizations was investigated inside a phantom by using artificial current sources and in patients by using a non–magnetic stimulation catheter. In addition, the effect of torso modeling on MCG dipole localization accuracy was thoroughly evaluated. In Section 4, calculation methods suitable for solving an equivalent current density are presented. These methods were developed and applied with simulated and measured MCG data. The uniform double layer (UDL) source model, which can be used in representing the spread

of the ventricular activation, was also studied by using invasively measured epicardial potential data for validation. The UDL model is described in Section 5. The main research centers currently involved in cardiomagnetic studies, especially the BioMag Laboratory at the Helsinki University Central Hospital (HUCH) where all the magnetic measurements analyzed in this thesis were performed, are presented in Section 6. Section 7 contains discussion about cardiomagnetic source imaging as well as it's future aspects.

2 Modeling of volume conductor and current source

In the following, the genesis of the bioelectric current sources inside the heart is briefly described. Thereafter, the well–known integral equations suitable for treating the problem in terms of bounding surfaces inside an inhomogeneous volume conductor (Barnard *et al* 1967a, 1967b, Geselowitz 1967, 1970, Horáček 1973) are presented. The formulation based on the bounding surfaces is needed in the calculations based on the boundary element method in which the surfaces are tessellated with geometrical elements. Finally, the concepts of the forward and the inverse problems are introduced. Since the inverse problem has no unique solution, the current source inside the heart is usually described with a source model, characterized by the values of the model parameters. The most commonly–used source models, applied in solving the cardiac inverse problem, will also be described. The source models investigated in this thesis and the estimation methods used in solving the values of the model parameters will be presented in the following sections.

2.1 Biolectric current sources and the activation of the heart

A cardiac cell at rest exposes a potential difference between the intra– and extracellular spaces so that the interior of the cell has a negative potential relative to the exterior. This potential difference is caused by the differences in the permeability of the cell membrane to different ions and by the ion pumps in the membrane. In the resting state, the cell membrane is rather permeable to potassium (K^+) ions whereas the permeability for the sodium (Na^+) ions is low. Therefore, the resting potential has a negative value close to the Nernst potential of K^+ ions, approximately between -80 mV and –95 mV. As a response to a stimulus, the permeability of the cell membrane to Na^+ ions increases. Thus, Na^+ starts to flow across the membrane causing the potential difference over the membrane to approach the Nernst potential of Na^+ which has a positive value. The amplitude of the change in the membrane voltage of a normal cardiac muscle cell is about 100 mV. The electrical activation results in the mechanical contraction of a muscle cell which is initiated by the influx of calcium (Ca^{2+}) ions, which further release Ca^{2+} ions inside the cell. The fast depolarization phase is followed by a plateau phase in the membrane potential, lasting approximately 200–300 ms. After the plateau phase, the membrane potential returns to it's original value. During the process, the cell is refractory, i.e. unable to respond to an additional electrical stimulus.

The activation cycle of a healthy heart is initiated by the sino–atrial (SA) node, located above the right atrium. In the special pacemaker cells of the SA node, the value of the membrane potential increases until the threshold for the opening of the Na^+ ion channels is reached. From the SA node, the electrical activation spreads along the internodal tracts in the atria thus depolarizing the atrial muscle cells. A phase of slow conduction is occurring in the atrio–ventricular (AV) node in the border of the atria and the ventricles. In the

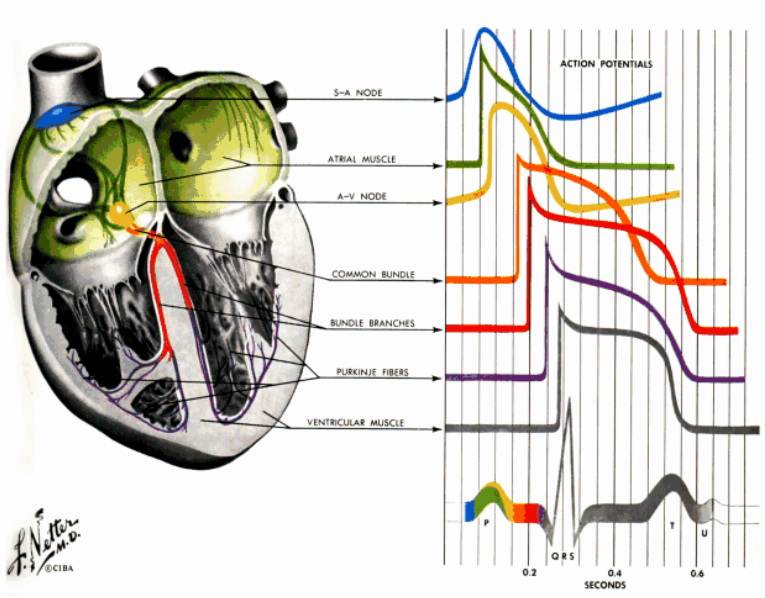

Fig. 1: *The time courses of the membrane potentials during the electrical excitation of the heart: the SA node, the atria, the AV node, the bundle of His, the bundle branches, the Purkinje fibers and the ventricular muscle (Netter 1991).*

ventricles, the activation spreads along the bundle of His, the right and left bundle branches and the Purkinje fibers which efficiently initiate the depolarization of the endocardial muscle cells. The excitation finally spreads from the endocardium towards the epicardium. The whole ventricular muscle is normally activated within 100 ms. The shapes of the membrane potentials in different types of cardiac cells is presented in Fig. 1, along with their timing with respect to an ECG signal measurable on the body surface. The form of the corresponding MCG signal closely resembles to the shape of the ECG signal. The activation of the atria causes the P–wave whereas the excitation of the ventricles causes the QRS–complex to appear in the ECG signal. The repolarization of the atria is hidden underneath the QRS–complex while the repolarization of the ventricles results in the T–wave.

The electric current flowing through the cell membrane is usually referred to as the microscopic *impressed current density* $\mathbf{J_i}$ (Plonsey 1969). The resulting magnetic field or the changes in the electric potential due to the impressed current flowing in one cardiac cell are too minor to be measured outside of the body. However, the activation in the heart spreads as a wavefront, and therefore several cells are activated simultaneously. When the macroscopic current distribution related to the activation of the heart is considered, it is customary to speak about the *primary current density* $\mathbf{J_p}$. The primary current density is restricted to the electrically active tissue (Tripp 1983), and it can be defined as the difference between the total current density $\mathbf{J_{tot}}$ and the passive, ohmic *volume current* $\mathbf{J_v}$: $\mathbf{J_p} = \mathbf{J_{tot}} - \mathbf{J_v}$. The volume current $\mathbf{J_v}$ is the result of the macroscopic electric field on charge carriers in the conducting medium (Hämäläinen and Nenonen 1999). The primary current is the target of

interest in solving the inverse problem. Because the volume current also contributes to the electric (**E**) and magnetic (**B**) fields, it has to be taken into account in the solutions.

2.2 Quasistatic approximation

As the total current density $\mathbf{J_{tot}}$ in the body is time–dependent, the generated electric and magnetic fields also vary with time. In the human body, the capacitive component of tissue impedance has been found to be negligible in the frequency band (< 1000 Hz) of internal bioelectric events (Plonsey 1969). Therefore, the time–varying electric potential and magnetic field in the human body can be assumed in most cases to behave as if they were *quasi–stationary*. According to this approximation, the true time–dependent field terms ($\partial\mathbf{E}/\partial t$, $\partial\mathbf{B}/\partial t$) in Maxwell's equations can be left out, and the quasi–static equations can be expressed as

$$\begin{aligned} \nabla \cdot \mathbf{E} &= \rho/\epsilon \ , & \nabla \times \mathbf{E} &= 0 \ , \\ \nabla \cdot \mathbf{B} &= 0 \ , & \nabla \times \mathbf{B} &= \mu_0(\mathbf{J_{tot}} + \nabla \times \mathbf{M}) \ , \end{aligned}$$

where ρ is the total charge density and $\epsilon = \epsilon_r\epsilon_0$, where ϵ_r is the relative electric permittivity of the medium and ϵ_0 is the electric permittivity of vacuum. The magnetic permeability of vacuum is denoted with μ_0 and the magnetization of the medium with **M**. Usually it is assumed that **M** has no effect on the field **B**.

The total current density $\mathbf{J_{tot}}$ can be divided into two components as explained before. The ohmic volume current relates directly to the electric field as $\mathbf{J_v} = \sigma\mathbf{E}$, where σ is the electric conductivity of the medium. Because the curl of the electric field vanishes, the electric field can be written as a gradient of a scalar potential $\mathbf{E} = -\nabla\phi$. Therefore, the total current density can be expressed as $\mathbf{J_{tot}} = \mathbf{J_p} - \sigma\nabla\phi$. Because the divergence of the total current density vanishes, the following Poisson equation is valid for a region containing primary sources:

$$\nabla \cdot \mathbf{J_p} = \nabla \cdot (\sigma\nabla\phi) \ . \tag{1}$$

If no primary sources are present, Eq. 1 turns into the Laplace equation $\nabla \cdot (\sigma\nabla\phi) = 0$. In a general case, the electric conductivity σ may be anisotropic, i.e. the conductivity varies as a function of direction. In such a case, σ in Eq. 1 can be expressed as a tensor.

The integral form of the curl equation for the magnetic field presents the Ampère–Laplace law:

$$\mathbf{B}(\mathbf{r}) = \frac{\mu_0}{4\pi}\int_{V'} \frac{\mathbf{J_{tot}}(\mathbf{r}\,') \times (\mathbf{r} - \mathbf{r}\,')}{|\mathbf{r} - \mathbf{r}\,'|^3}\, dv' \ , \tag{2}$$

where $\mathbf{r}$ is the observation (field) point, $\mathbf{r}\,'$ is the integration (source) point, and the integration volume V' contains all sources. By including the separation of the total current into primary and volume current components, Eq. 2 can be expressed as (Geselowitz 1970)

$$\mathbf{B}(\mathbf{r}) = \frac{\mu_0}{4\pi}\int_{V'} (\mathbf{J_p}(\mathbf{r}\,') + \phi(\mathbf{r}\,')\nabla'\sigma(\mathbf{r}\,')) \times \frac{(\mathbf{r} - \mathbf{r}\,')}{|\mathbf{r} - \mathbf{r}\,'|^3}\, dv' \ . \tag{3}$$

Eq. 3 shows that in the case of an infinite homogeneous volume conductor, the second term in the integral vanishes, and the magnetic field depends only on the primary current. Also in special kind of bounded volume conductors, such as a sphere and an infinite half–space, the radial component of the magnetic field, which is usually to be measured, is unaffected by the conductivity difference over the bounding surface. The sphere model is often applied in brain studies, and the infinite half–space has been used, e.g., to approximate the anterior surface of the torso in heart studies.

In the general case, the volume conductor may contain regions with different and even anisotropic electric conductivities. In such a case, the electric potential and the magnetic field in the whole volume conductor will have to be solved from Eqs. 1 and 2, e.g., with the *finite element method* (FEM) (e.g., Czapski *et al* 1996 and Klepfer *et al* 1997) or with the *finite difference method* (FDM). In cardiomagnetic source imaging studies, however, the volume conductor is usually modeled as *piecewise homogeneous*. In this case, the *boundary element method* (BEM) (e.g., Brebbia *et al* 1984) can be used in the calculations. In BEM, the computational demands will be smaller than in FEM or FDM. The BEM is used throughout this thesis.

2.3 Piecewise homogeneous volume conductor

In the following, we assume a piecewise homogeneous volume conductor consisting of M different regions. Each region has a constant and isotropic conductivity, σ_k, and is bounded by the surface S_k. In this case, the gradient of the conductivity vanishes everywhere else except at the borders of the regions, and the volume integral of the second term in Eq. 3 can be turned into a surface integral (Geselowitz 1970):

$$\mathbf{B}(\mathbf{r}) = \mathbf{B}_\infty(\mathbf{r}) - \frac{\mu_o}{4\pi}\sum_{k=1}^{M}(\sigma_k' - \sigma_k'')\int_{S_k}\phi_{S_k}\mathbf{dS_k}\times\frac{(\mathbf{r}-\mathbf{r}\,')}{|\mathbf{r}-\mathbf{r}\,'|^3}\ , \tag{4}$$

where σ_k' and σ_k'' are the conductivities inside and outside of the surface S_k, respectively. The primary current density $\mathbf{J_p}$ produces the magnetic field $\mathbf{B}_\infty$ in an infinite homogeneous volume conductor, and $\mathbf{dS_k} = \mathbf{n}\ dS_k$ is a vector element of surface S_k, oriented along the outward unit normal $\mathbf{n}$.

The electric potential ϕ_{S_l} on the surface S_l in a piecewise homogeneous volume conductor can be obtained from Eq. 1 by applying the proper boundary conditions and by using the Green's theorem (Barnard *et al* 1967a, 1967b, Geselowitz 1967, Horáček 1973):

$$\phi_{S_l}(\mathbf{r}) = \frac{2\sigma_s}{(\sigma_l' + \sigma_l'')}\phi_\infty(\mathbf{r}) - \frac{1}{2\pi}\sum_{k=1}^{M}\frac{(\sigma_k' - \sigma_k'')}{(\sigma_l' + \sigma_l'')}\int_{S_k}\phi_{S_k}\mathbf{dS_k}\cdot\frac{(\mathbf{r}-\mathbf{r}\,')}{|\mathbf{r}-\mathbf{r}\,'|^3}\ , \tag{5}$$

where σ_s is the electric conductivity at the source location and ϕ_∞ the electric potential in an infinite homogeneous volume conductor. The conductivity on the surface S_l is defined as

the average of the conductivities inside and outside of the surface: $\sigma_{S_l} = \frac{1}{2}(\sigma_l'' + \sigma_l')$. Since the unknown potential functions are inside the integrand, Eqs. 4 and 5 are not analytically solvable in a general case. However, they can be solved numerically with the BEM. The boundary element (BE) torso models used in the MCG inverse calculations typically contain at least the surface of the torso. Improvements in the torso models can be obtained by including the lungs and the intraventricular blood masses. The torso models can be reconstructed, e.g., from magnetic resonance (MR) images. Recently, automated methods have been developed for the reconstruction of BE models (Lötjönen 2000). The modeling of the volume conductor will be further addressed in section 3.5.

2.4 Boundary element approximation

In the boundary element method, an approximate solution $\tilde{\phi}$ for the potential on the bounding surfaces can be obtained by representing the surfaces in simplified forms and by approximating the potential with a set of basis functions. The bounding surfaces, separating the regions with different conductivities, are tessellated with geometrical elements. This reduces the surface integrals in Eqs. 4 and 5 to summations of surface integrals over the elements. The approximate solution $\tilde{\phi}$ is defined as a linear combination of N_f basis functions, denoted by $h_1, \cdots, h_{N_f}$, such that

$$\tilde{\phi}(\mathbf{r}) = \sum_{i=1}^{N_f} \alpha_i h_i(\mathbf{r}) \ , \tag{6}$$

where α_i are scalar coefficients and $\mathbf{r}$ is a point on one of the bounding surfaces. The sum of the basis functions in any $\mathbf{r}$ is restricted to one.

Flat triangular elements, denoted as Δ_i, are most commonly used in the biomagnetic calculations. With these elements, *constant* or *linear* potential approximations can be applied which have also been used in this thesis. Higher–order elements, such as curved triangles (Frijns *et al* 2000, Gençer and Tanzer 1999) and 8–noded isoparametric quadrilateral elements (Wach *et al* 1997, Fischer *et al* 1998, 1999a), have also been introduced in the literature. A brief description of the different approximations will be given in the following.

2.4.1 Constant potential approach

In the constant potential approximation, the center points of the triangles are used as the discretization points. The potential is assumed to be constant over each triangle, resulting in the most simple set of basis functions:

$$h_i(\mathbf{r}) = \begin{cases} 1 & \text{if } \mathbf{r} \in \Delta_i \\ 0 & \text{otherwise} \end{cases} \ . \tag{7}$$

Therefore, the integration in Eqs. 4 and 5 can be reduced to summations over the constant potential values, multiplied by the *solid angle* factors $\Omega_{ij} = -\frac{1}{2\pi} \int_{\Delta_j} \mathbf{n}_j d\Delta_j(\mathbf{r}\,') \cdot \frac{\mathbf{c}_i - \mathbf{r}\,'}{|\mathbf{c}_i - \mathbf{r}\,'|^3}$,

where Ω_{ij} is the solid angle (divided by 2π) subtended by the triangle Δ_j at the centroid $\mathbf{c}_i$ of triangle Δ_i, and $\mathbf{n}_j$ is the outward unit normal of triangle Δ_j. The value of the solid angle for a plane triangle can be calculated analytically (van Oosterom and Strackee 1983), and Eq. 5 can be discretized into

$$\boldsymbol{\phi}^l = \mathbf{g}^l + \sum_{k=1}^{M} \omega^{lk} \boldsymbol{\phi}^k, \quad l = 1, \ldots, M \ , \tag{8}$$

where the vectors $\boldsymbol{\phi}^l$ and $\mathbf{g}^l$ contain the values ϕ_i^l and $g_i^l = (2\sigma_s \phi_{\infty,i}^l)/(\sigma_l^{''} + \sigma_l^{'})$ in each triangular element Δ_i^l of the surface S_l. The matrices ω^{lk} are composed as follows:

$$\omega_{ij}^{lk} = \begin{cases} \frac{\sigma_k^{'} - \sigma_k^{''}}{\sigma_l^{''} + \sigma_l^{'}} \Omega_{ij} & \text{if } i \neq j \\ 0 & \text{if } i = j \end{cases} \ . \tag{9}$$

The formulation in Eq. 8 for all the surfaces can be expressed as a matrix equation (Nenonen *et al* 1991a, Purcell and Stroink 1991)

$$(I - \Omega)\boldsymbol{\Phi} = \mathbf{G} \ , \tag{10}$$

where the vectors $\mathbf{G}$ and $\boldsymbol{\Phi}$ contain the infinite and bounded potential values in all triangles, I is the identity matrix and Ω is composed of the matrices ω^{lk}. However, the matrix $(I - \Omega)$ is singular, and no unique solution can be derived for $\boldsymbol{\Phi}$ from Eq. 10. The technique of multiple deflations (Lynn and Timlake 1968) is needed to alter the matrix $(I - \Omega)$ so that the singularity is removed and the matrix can be inverted. Thereafter, a modified solution $\tilde{\boldsymbol{\Phi}}$ for the bounded potential values can be obtained from

$$\tilde{\boldsymbol{\Phi}} = (I - \tilde{\Omega})^{-1}\mathbf{G} \ , \tag{11}$$

where $(I - \tilde{\Omega})$ denotes to the deflated matrix. Thereafter, reflation is needed to obtain the true potential values on the inner surfaces. The body surface potentials do not need to be reflated.

The surface integrals in Eq. 4 can be discretized with the constant potential approach as follows:

$$\int_{S_k} \phi_{S_k} \mathbf{dS_k} \times \frac{(\mathbf{r} - \mathbf{r}\,')}{|\mathbf{r} - \mathbf{r}\,'|^3} \approx \sum_{j=1}^{n_k} \phi_j^k a_j \mathbf{n}_j \times \frac{(\mathbf{r} - \mathbf{c}_j)}{|\mathbf{r} - \mathbf{c}_j|^3} \ , \tag{12}$$

where n_k is the number of elements representing the surface S_k and a_j is the area of triangle Δ_j^k. Thereafter, Eq. 4 can be written as a matrix equation. By including the bounded potential values the result is (Nenonen *et al* 1991a)

$$\mathbf{B} = \mathbf{B}_\infty + C\boldsymbol{\Phi} \ . \tag{13}$$

Eqs. 11 and 13 provide the means to include the effect of boundaries in a piecewise homogeneous volume conductor. The matrix $(I - \tilde{\Omega})^{-1}$ depends only on the geometry of the volume

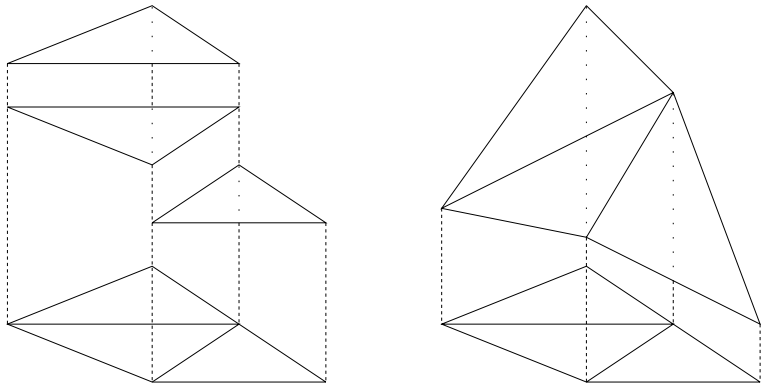

(a) (b)

Fig. 2: *The BE potential approximations used in this thesis, showing a) constant values of potential over each surface triangle and b) linearly varying potentials.*

conductor, and therefore does not need to be calculated again if the geometry remains the same. The matrix C also contains the locations of the measuring sensors, and therefore needs to be updated if the sensor configuration changes. A schematic view of the constant potential approximation is presented in Fig. 2a.

2.4.2 Linearly varying surface potentials

Another more recent approach is to let the surface potential vary linearly over each triangle. In this case, the basis functions are defined as follows (de Munck 1992):

$$h_i(\mathbf{r}) = \begin{cases} \frac{\det\ (\mathbf{r},\mathbf{r}_j,\mathbf{r}_k)}{\det\ (\mathbf{r}_i,\mathbf{r}_j,\mathbf{r}_k)} & \text{if } \mathbf{r} \in \Delta_i^{jk} \\ 0 & \text{otherwise} \end{cases} , \tag{14}$$

where det denotes to the determinant and Δ_i^{jk} to any triangle for which $\mathbf{r}_i$ is a node; the other two nodes are noted by $\mathbf{r}_j$ and $\mathbf{r}_k$. The basis functions defined in Eq. 14 equal to one at the node $\mathbf{r}_i$, and drop linearly to zero while approaching the edge $\mathbf{r}_k - \mathbf{r}_j$. An analytic formulation for the surface integrals in Eq. 5 in case of linearly varying surface potentials has been presented by de Munck (1992). Thereafter, Ferguson *et al* (1994) presented an analytic derivation of the surface integrals in Eq. 4. In the linear formulation, the solid angles subtended by triangles for which the observation point is a node are usually treated separately. The treatment is based on the fact that the solid angle subtended by a smooth, closed surface at a point on the surface equals to -2π. Therefore, the remaining solid angle can be distributed between the observation node and the neighboring nodes in matrix Ω.

As the number of nodes equals approximately to one half of the number of triangles, the size of the matrix Ω in the linear case reduces to one fourth with respect to the constant potential approach. The accuracy of constant vs. linear potential approximation in calculating body surface potentials has been investigated by Ferguson and Stroink (1997). They

found that in general, the linearly varying surface potentials produce more accurate solutions. However, a study about the effect of constant vs. linear approximation in the MCG forward and inverse calculations has not yet been published. In this thesis, both constant and linear approximations have been used in the calculations.

2.4.3 Higher–order elements

The flat triangle elements can be turned into higher–order elements, such as quadratic or cubic (e.g., Gençer and Tanzer 1999), by adding discretization points in the triangles. In such cases, the basis functions as well as the elements will have second– or third–order shapes. This is called isoparametric formulation which means that both variation in the geometry of an element and the potential function on it are defined with the same interpolation functions. The surface integration over the elements is then done numerically. Eight–noded isoparametric quadrilateral elements have been used, e.g., by Wach *et al* (1997) and by Fischer *et al* (1998) in calculating the transmembrane potential distribution on the surface of the heart. Fischer *et al* (1999a) have compared different basis functions applicable with eight–noded quadrilateral elements. They found that the use of so–called serendipity basis functions is likely to cause local oscillations in the solution while the basis functions based on complete second–order Lagrange polynomials produce more stable solutions. However, the effect of higher–order elements on the numerical accuracy of the field calculations is still unclear; inaccuracies, e.g., in the numerical integration may erase the improvements obtained by the more accurate discretization of the bounding surfaces. On the other hand, if the source is located close to a bounding surface, the higher–order functions might be beneficial due to their variation over the element. In this case, constant or linear potential approximation could cause numerical errors in the calculations.

2.5 Modeling of the current source

In source localization studies, the *forward problem* has to be solved first, i.e. one has to solve the electromagnetic field on the surface and outside of the body for the selected source and volume conductor models. The *inverse problem* in electro– and magnetocardiography involves the estimation of the electrical activity of the heart from measured body surface potential and magnetic field values, respectively. As the magnetic field outside of the body, or the potential distribution observed on the surface of the body, can be generated by an infinite number of distinctive source distributions inside the heart, there is no unique solution to the inverse problem on the basis of the measured ECGs or MCGs alone; a restrictive model describing the current source is needed. The solution to the inverse problem is then obtained by minimizing the difference between the measured data and the data produced by the existent values of the source model parameters. In the following, the most commonly–

used source models in cardiac inverse studies are briefly reviewed. The source models used in this thesis will be more thoroughly introduced in the following sections.

2.5.1 Point–like source models

The most commonly used source model in solving the inverse problem of magnetocardiography is the *equivalent current dipole*, ECD (e.g., Cohen and Hosaka 1976, Savard *et al* 1980, Purcell *et al* 1988, Nenonen *et al* 1991a, Hren *et al* 1996). The ECD can be described with six parameters: three location coordinates and three dipole moment components, and it is restricted to only one point in space

$$\mathbf{J_p}(\mathbf{r}\,') = \mathbf{Q}\delta(\mathbf{r}\,' - \mathbf{r}_Q) \;, \tag{15}$$

where $\mathbf{Q}$ is the moment and $\mathbf{r}_Q$ the location of the ECD. The ECD is the first term of the multipole expansion for the magnetic field which can be derived from the magnetic vector potential $\mathbf{A_p}$ related to the primary current distribution $\mathbf{J_p}$ (Katila and Karp 1983)

$$\mathbf{A_p}(\mathbf{r}) = \frac{\mu_0}{4\pi} \int_{V'} \frac{\mathbf{J_p}(\mathbf{r}\,')}{|\mathbf{r} - \mathbf{r}\,'|}\, dv' \;. \tag{16}$$

The magnetic field can be obtained from the total magnetic vector potential $\mathbf{A}$ as $\mathbf{B} = \nabla \times \mathbf{A}$, where $\mathbf{A} = \mathbf{A_p} + \mathbf{A_v}$, and $\mathbf{A_v}$ is the vector potential related to volume currents. However, the magnetic field in a homogeneous volume conductor, or the radial component of the field in an infinite half–space, can be obtained from the vector potential in Eq. 16. To obtain the multipole expansion, the denominator inside the integral in Eq. 16 is expressed as a Taylor series:

$$\mathbf{A_p}(\mathbf{r}) = \frac{\mu_0}{4\pi r} \int_{V'} \mathbf{J_p}(\mathbf{r}\,')\, dv' + \frac{\mu_0}{4\pi r^3}\, \mathbf{r} \cdot \int_{V'} \mathbf{r}\,' \mathbf{J_p}(\mathbf{r}\,')\, dv' + \ldots \;, \tag{17}$$

where the first term contains the dipole and the second the quadrupole component of the multipole expansion. The current dipole studies will be described in detail in Section 3. Other point–like source models are the higher–order terms of the multipole expansion, such as the quadrupole and the octupole, and the magnetic dipole (e.g., Katila *et al* 1987, Nenonen *et al* 1991b, Mäkijärvi *et al* 1992). If the primary current is confined into a small volume of cardiac tissue, the use of point–like source models is physiologically justified, such as in localizing the onset of the ventricular activation. However, when the activation starts to spread in the cardiac muscle, the assumption about a small current source region is no longer good.

2.5.2 Distributed source models

Distributed source models have been developed for describing the bioelectric current sources in a more realistic way than is possible with point–like source models. A source model based on representing the primary current distribution with an equivalent current density

was introduced by Hämäläinen and Ilmoniemi (1984). The applied calculation methods and the results obtained in this thesis by using the equivalent current density will be presented in Section 4.

Another source model, developed during the past 15 years at the University of Nijmegen (Huiskamp and van Oosterom 1988), is the Uniform Double Layer (UDL). It describes the activity of the heart during ventricular depolarization in terms of the activation times at the epicardial and endocardial ventricular surfaces. The UDL model has also been investigated in this thesis, and it will be presented more thoroughly in Section 5.

A popular and widely applied source model, suitable for solving the inverse problem of electrocardiography, is the epicardial (or pericardial) potential distribution (e.g., Barr *et al* 1977, Rudy and Messinger–Rapport 1988, Shahidi *et al* 1994, Horáček and Clements 1997, Oster *et al* 1997). It has been used as an equivalent generator for the body surface potentials on the basis of a one–to–one relationship between the body surface potential and the potential on the epicardial surface (Yamashita and Geselowitz 1985). Despite the theoretical uniqueness between the two potential distributions, the discrete sampling on the body surface and the smoothing properties of the volume conductor cause the problem of solving the epicardial potential distribution from body surface potentials to be *ill–posed*, i.e. sensitive to even small amounts of noise in the measured data. The concept of ill–posedness, as well as the mathematical means for obtaining a stable solution for an ill–posed problem, will be addressed in detail in Section 4.

The transmembrane potential distribution over the surface of the heart has also been used to model the cardiac electrical activity (e.g., Wach *et al* 1997, Fischer *et al* 1998, 1999a). This source model can be derived from the bidomain model of the heart (e.g., Geselowitz and Miller 1983). In the bidomain model, the cardiac muscle is considered to consist of an intracellular and an extracellular domain where current passes from one domain to the other through the cell membrane. The transmembrane potential ϕ_m is defined as the potential difference between the intra– and extracellular space: $\phi_m = \phi_i - \phi_e$. If the anisotropic electric conductivity of the cardiac muscle is taken into account, the electric potentials in the extracellular domain are associated with current sources proportional to the spatial gradient of ϕ_m inside and on the surface of the heart (Geselowitz and Miller 1983). Hence, from a given ϕ_m throughout the myocardium, one can calculate the electric potential and the magnetic field on and outside of the body surface, respectively. If equal anisotropy ratios in the intra– and extracellular domains are assumed, the volume contribution vanishes and the potential outside of the heart can be expressed as a function of the transmembrane potential on the surface of the heart (Yamashita and Geselowitz 1985).

3 Current dipole localization

The equivalent current dipole (ECD) has been widely applied in the inverse problem of MCG due to it's simplicity. It has been proven successful in locating early activation sites, especially an accessory pathway between the atria and the ventricles in the Wolff–Parkinson–White (WPW) syndrome, and the origin of ectopic beats and arrhythmia. In addition to MCG studies, the ECD has also been applied in multichannel BSPM measurements. In the following, the calculation methods used in the ECD localization are first introduced. Thereafter, the results obtained with the ECD are described, proceeding from simulation to clinical studies. In the end, the effect of volume conductor modeling is addressed.

3.1 Calculation methods

Previously, current dipole localizations have been carried out by minimizing the contribution of the higher–order terms of the multipole expansion presented in Eq. 17. The dipole location was obtained as the site where the quadrupole contribution to the observed potentials or the magnetic field was minimized. This technique has been described, e.g., by Cuffin and Geselowitz (1977) and Savard *et al* (1982), and applied in clinical studies by Gulrajani *et al* (1984) and Savard *et al* (1985).

Nowadays current dipole localizations are carried out by assuming that the current source is composed of a dipole only. The calculations are most commonly performed with a non–linear least squares optimization algorithm, known as the Levenberg–Marquardt (LM) algorithm (Marquardt 1963). The LM–algorithm has been used in this thesis, and it requires an initial guess for the dipole parameters. The values of the parameters are then used to generate the forward solution. Thereafter, the dipole is shifted and scaled to minimize the residual between the measured and computed MCG maps. The squared residual is often referred to as the biomagnetic cost function. Dipole localizations can also be calculated with the Simplex method (see e.g., Press *et al* 1993).

The quality of the ECD localizations can be assessed, e.g., with the *goodness of fit value*, g, which measures the similarity between the measured and the calculated magnetic field over all m sensors:

$$g = 1 - \frac{\sum_{i=1}^{m}(B_i - \tilde{B}_i)^2}{\sum_{i=1}^{m} B_i^2} \ , \tag{18}$$

where B_i denotes the measured and $\tilde{B}_i$ the calculated magnetic field at the ith sensor, respectively. A high goodness of fit value indicates that the non–dipolar components of the data are negligible, and thus the localizations can be expected to be accurate. The required accuracy of ECD localizations is strongly dependent on the application; an accuracy of 10 mm could be considered adequate for most clinical purposes. However, the result should be in the correct anatomical region of the heart.

The problem in the LM–algorithm is that, e.g., in the presence of measurement noise or bounding surfaces close to the current source, the biomagnetic cost function can have multiple minima where the algorithm can converge to. In this case, the solution of the LM–algorithm will depend on the initial values of the parameters which have to be close to the true values to obtain a correct solution. So–called global approaches in ECD localization have been proposed as solutions to this problem. In the method suggested by Scholz and Schwierz (1994), the concept of locally optimal dipoles was presented. Solving the dipole moment was separated from the calculation, and thus the biomagnetic cost function became dependent on the location of the dipole only. The whole solution space was then scanned through, and the global minimum of the cost function was selected to be the true solution. Thereafter, the components of the dipole moments were obtained by a linear fit from the measured data.

Uutela *et al* (1998), in turn, investigated three global optimization methods in fitting a multidipole model to neuromagnetic data: clustering, simulated annealing and genetic algorithms. The genetic algorithm was found to be superior to the two other methods. However, using a global localization scheme is considerably more time consuming than the iterative LM–algorithm.

3.2 Simulation studies

The accuracy of the ECD localizations has been the subject of investigation in several simulation studies regarding the inverse problem of magnetocardiography. Most studies are related to the effect of the torso model on the localization accuracy. Such studies will be discussed in more detail in section 3.5. In a recent simulation study investigating the applicability of the ECD as the source model, Hren *et al* (1998) positioned pre–excitation sites on the epicardial surface along the AV ring of an anatomical model of the human ventricular myocardium. Electric potential and magnetic field distributions were then simulated on and outside of the torso model, respectively. They found that with an accurate torso description and with a realistic amount of measurement noise, a minimum in the ECD localization error (7 ± 3 mm both for MCG and BSPM) was achieved 20 ms after the onset of pre–excitation. Later in the activation sequence, the effects of the size and the shape of the activation wavefront started to reduce the ECD localization accuracy.

3.3 Phantom and animal studies

The accuracies of MCG and BSPM dipole localizations have also been studied with phantom experiments. In a phantom study by Moshage *et al* (1996), the measurements were done with a plexiglass tank (size: 40 cm $\times$ 40 cm $\times$ 25 cm) together with bipolar and quadrupolar stimulation catheters. The infinite halfspace was used as the volume conductor model. At

source–dewar distances between 8 cm and 20 cm, the ECD localization errors were reported to be between 5 mm and 30 mm.

In Publication I, artificial dipolar sources inside a physical thorax phantom were applied to experimentally investigate the obtainable accuracy of the magnetocardiographic ECD localizations. For the measurements, the phantom was filled with saline solution with an electric conductivity of 0.21 S/m which corresponds to the average conductivity of the human thorax (Geddes and Baker 1967). The 67–channel cardiomagnetometer at the BioMag Laboratory, located at HUCH, was employed in recording magnetic signals generated by seven dipolar sources located from 25 mm to 145 mm below the surface of the phantom. The signal–to–noise ratio (SNR) and the goodness of fit of the localizations were used in assessing the quality of the results. In Publication I, the expected dependence between the SNR and the goodness of fit was derived to be

$$g \approx 1 - \frac{1}{SNR^2} \ , \tag{19}$$

and the results were found to correspond to Eq. 19. With the SNR between 5 and 10, the average localization error was found to be 9 ± 8 mm, while for the SNR between 30 and 40 and for the goodness of fit between 99.5 % and 100 %, the average error reduced to 3.2 ± 0.3 mm. However, in patient measurements Eq. 19 might not hold due to systematic model errors or to correlated noise in the data. In Figs. 3a and 3b, the BE model of the phantom and the source positions are presented. The average localization errors and the standard deviations of the errors are presented in Figs. 3c and 3d. The results show an improvement in the accuracy with increasing values of SNR and goodness of fit.

In a phantom study by Fenici *et al* (1998), the accuracies of both MCG and BSPM dipole localizations were investigated by using a non–magnetic stimulation catheter (Fenici *et al* 1996). The average MCG localization accuracy was 2–7 mm while the average BSPM localization accuracy was 4–10 mm, depending on the depth of the source. The phantom study was performed using the same non–magnetic catheter as was used in patient measurements in Publications II and III. Therefore in a phantom, the MCG and BSPM dipole localization accuracies were found to be of the same order. In a phantom study by Tenner *et al* (1999), the effects of cylindrical inhomogeneities, representing the lungs, were studied by calculating MCG and BSPM dipole localizations. They found that the localizations were typically distorted by 5–10 mm when the inhomogeneities were discarded from the BE model. In addition, 10–30 % errors were found in the estimated dipole amplitudes.

The accuracy of BSPM dipole localizations has also been studied from experimental setups. Savard *et al* (1980) performed an *in vivo* animal study, using the ECD as the source model together with a numerical dog torso model to determine the site of induced ectopic activity in the intact dog. The average distance between the localizations and the sites of ectopic activity was found to be 19 ± 8 mm.

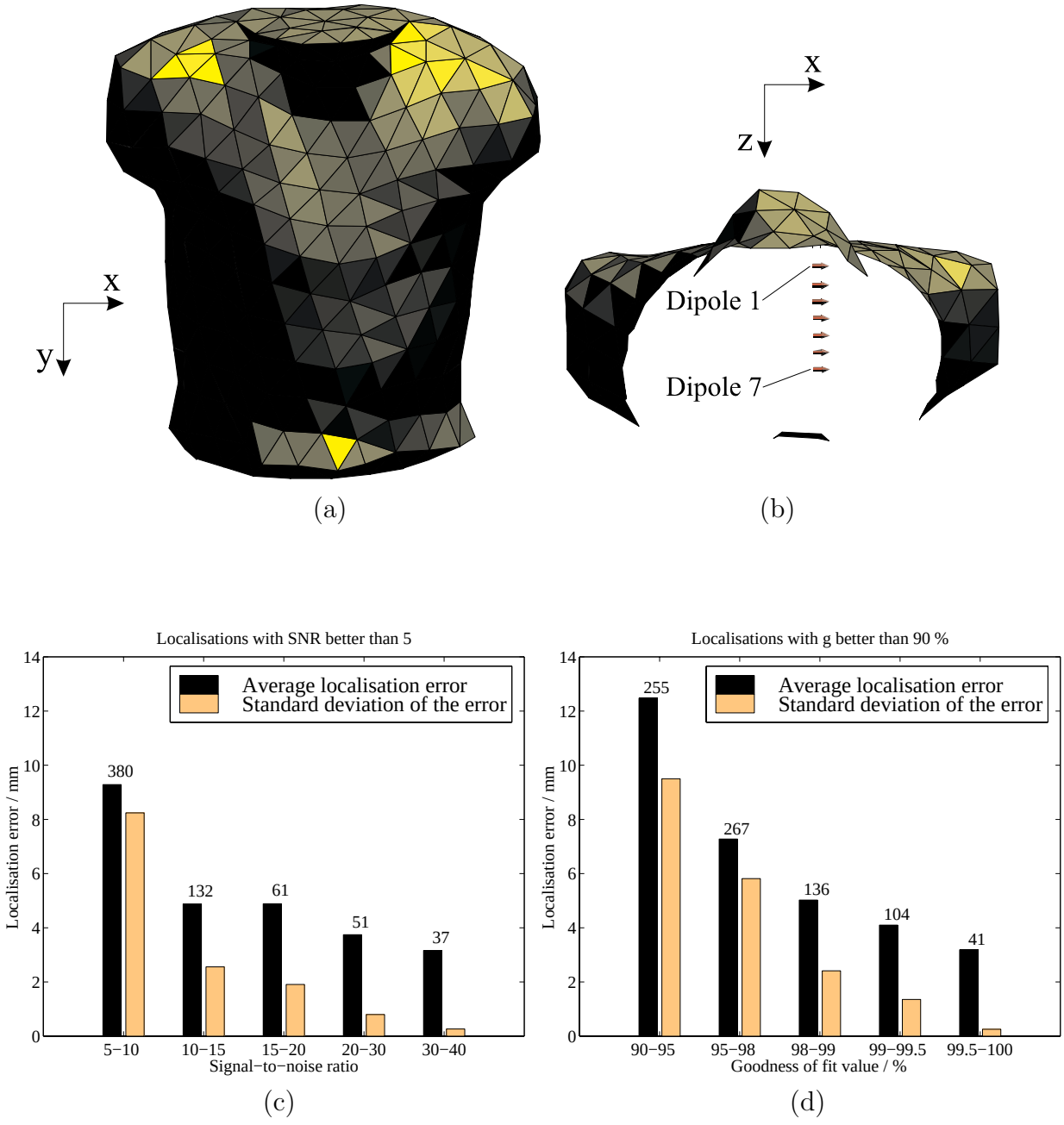

Fig. 3: *a) The anterior projection and b) the transaxial projection of the BE model of the phantom together with the positions of the seven dipolar current sources. The mean localization errors calculated in certain ranges of c) SNR and d) goodness of fit. Only the localizations with the SNR or the goodness of fit belonging to the selected ranges displayed on the x–axis were included in the calculation. The average errors are plotted by black bars and the standard deviations of the errors by gray bars. The number of localizations belonging to each range is displayed on top of the bars. (From Publication I)*

3.4 Patient measurements

The ECD has been widely applied in clinical MCG and BSPM source localization studies. In the following, results from some of these studies are briefly reviewed. Gulrajani *et al* (1984) used the ECD to localize the accessory pathway from 26–channel BSPM measurements in 28 WPW–patients. They found that the ECD solutions could not separate the accessory pathway sites into eight AV locations, however, right–sided, posterior and left–sided pre–excitation could be separated. Savard *et al* (1985) calculated ECD localizations from 63 BSPM leads in 14 patients with implanted pacemakers. The localized sites were found to be within 25 ± 12 mm from the pacing leads.

In MCG studies, Nenonen *et al* (1991a) used the ECD to localize the pre–excitation sites in 10 WPW–patients. The MCG measurements were performed with a single–channel device. They found an average accuracy of 22 ± 10 mm by scaling a standard homogeneous BE torso model to approximate the true shape of the subjects. Mäkijärvi *et al* (1992) applied the ECD, as well as the quadrupole and the magnetic dipole, in localizing ventricular pre–excitation sites in 15 WPW–patients. By modeling the volume conductor with an infinite half–space they obtained an accuracy of 73 mm for the ECD, indicating the need for a more realistic representation of the torso. Weismüller *et al* (1992) localized accessory pathways from 37–channel MCG recordings in seven WPW–patients. In their study, the results showed an average accuracy of 21 mm with respect to invasive catheter mapping. Nenonen *et al* (1993) localized accessory pathways in 12 WPW–patients using a standard homogeneous torso model. The average 3D difference between the MCG and the invasive results was 21 ± 9 mm. Bruder *et al* (1994a) localized accessory pathways in two WPW–patients, ectopic activation from two ventricular extrasystoles and two (a shallow and a deep) catheter positions. An average accuracy of 24 mm was obtained by individual scaling of a standard homogeneous torso model. Oeff and Burghoff (1994) investigated 18 WPW–patients prior to catheter ablation and five coronary artery disease (CAD) patients with a sufficient number of monomorphic ventricular extrasystoles to enable evaluation. The MCG results were compared to the site of successful catheter ablation, and an average difference of 21 ± 17 mm was found. In the CAD patient group, the origin of the ventricular premature beats was localized in four patients at the border of infarcted areas. Moshage *et al* (1996) found an ECD localization accuracy of 18 ± 5 mm in 19 patients with ventricular arrhythmias with respect to electrophysiological (EP) mapping. In six patients with a non–magnetic pacing catheter, the stimulus spike was localized within 12 mm from the position determined from MR images.

In Publication II, the MCG localization accuracy was investigated in five patients using a non–magnetic stimulation catheter (Fenici *et al* 1996). After standard EP studies, the catheter was placed in four cases in the right ventricle (RV) and in one case in the coro-

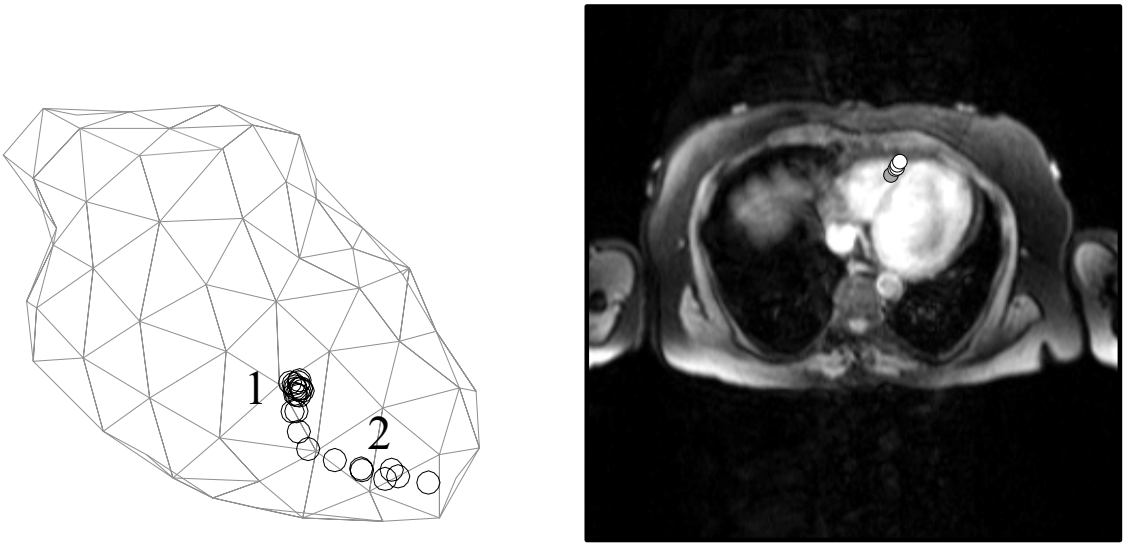

(a) (b)

Fig. 4: *a) A triangulated epicardial surface of a patient in Publication II, showing the ECD localizations of the tip of the catheter and the cardiac evoked field (1) 3–15 ms and (2) 15–30 ms after the stimulus. b) A transaxial MR image of the heart of the same patient, showing the localization of the tip of the catheter (gray circle) and the resulting evoked response 3–10 ms later (white circles). (From Publication II)*

nary sinus (CS). The position of the catheter was documented in biplane cine X–ray images. Thereafter, MCG signals were recorded during cardiac pacing in the shielded room of the BioMag Laboratory. The artificial current dipole in the tip of the catheter stimulates myocardial cells located near to the tip. Therefore, the resulting cardiac activation originates from the vicinity of the tip. The myocardial activation following a stimulus current pulse is referred as the *myocardial evoked response*, which in turn produces a magnetic *cardiac evoked field* (CEF). Non–invasive localizations of the tip of the catheter and the myocardial evoked responses were computed from the measured MCG data using patient–specific homogeneous BE torso models. The mean distance between the tip of the catheter, determined from fluoroscopy, and MCG localizations during the stimulus spikes was 11 $\pm$ 4 mm. The mean distance between the localizations calculated during the stimulus spikes and in the beginning of the CEFs was 4 $\pm$ 1 mm, as determined from signal–averaged data. The propagation velocity of the ECDs between 5 ms and 10 ms after the stimuli was found to be 0.9 $\pm$ 0.2 m/s. An example of the localization results reported in Publication II is presented in Fig. 4. The accurate 3D localizations of the tip of the catheter suggest that the MCG method could be developed towards a useful clinical tool during EP studies.

Only a few studies have been presented with localizations from simultaneous MCG and BSPM measurements. Bruder *et al* (1994b) have investigated the accuracy of dipole localizations from simultaneously recorded 37–channel MCG and 40–channel BSPM data of two patients with the WPW syndrome. In their study, the validation was provided by the sites of

successful catheter ablation. The MCG and BSPM accuracies were found to be 20–30 mm. In Publication III, the accuracy of ECD localizations was comprehensively studied for the first time by using the non–magnetic catheter as a reference current source. The validation for the localizations was obtained by documenting the position of the tip of the catheter on biplane fluoroscopic images. Multichannel MCG and BSPM measurements in 10 patients were then carried out by pacing the heart in the shielded room of the BioMag Laboratory. The myocardial evoked response reflected as the CEF in the magnetic data and as the *cardiac evoked potential* (CEP) in the body surface potential recordings. An example of the data used in Publication III is presented in Fig. 5. The ECD localizations were calculated using individual homogeneous and inhomogeneous BE torso models. Using MCG data, an average 3D localization accuracy of 7–9 mm was obtained which can be considered sufficient for guiding ablative procedures in a catheterization laboratory. The average BSPM localization accuracy obtained in this study was considerably lower, only 25–31 mm. Typically, the BSPM localization results overestimated the depth of the source.

3.5 Effect of torso modeling

Several studies applying the ECD have been reported concerning the effect of inhomogeneities in the BE model. Solving the forward problem shows the changes in the morphological patterns of the MCG and BSPM data, due to changing the properties of the volume conductor model. Horáček *et al* (1987) assessed how the geometry and the composition of the torso affect the extracorporal magnetic field, produced by a current dipole in the center of the ventricular mass. They found that the intraventricular blood masses caused a noticeable rotation of the maps' extrema. Both lungs and blood masses tended to swing the distribution towards a field pattern that would have been caused by a dipole oriented along the anatomical axis of the heart. Purcell *et al* (1988) found that the outer boundary of the torso and the intracavitary blood masses had the largest effect on the electric and magnetic field produced by a single current dipole placed at various locations in the heart. Bruder *et al* (1994b) found as well that the outer boundary of the torso had the major influence on both BSPM and MCG maps, and that the influence of the lungs was smaller than that of the blood masses.

In the inverse problem studies, Forsman *et al* (1992) found that the magnetocardiographic ECD localizations of deep current sources can be distorted even by several centimeters by discarding the inhomogeneities (lungs, blood masses) from the torso model. Tan *et al* (1992) investigated the effect of scaling the torso model and found that by using scaling factors of 0.9–1.1, the effect on the localization accuracy was typically less than 10 mm for dipoles tangential to the anterior surface of the torso. For a perpendicular dipole, the results were affected even by several centimeters. Bruder *et al* (1994b) also investigated

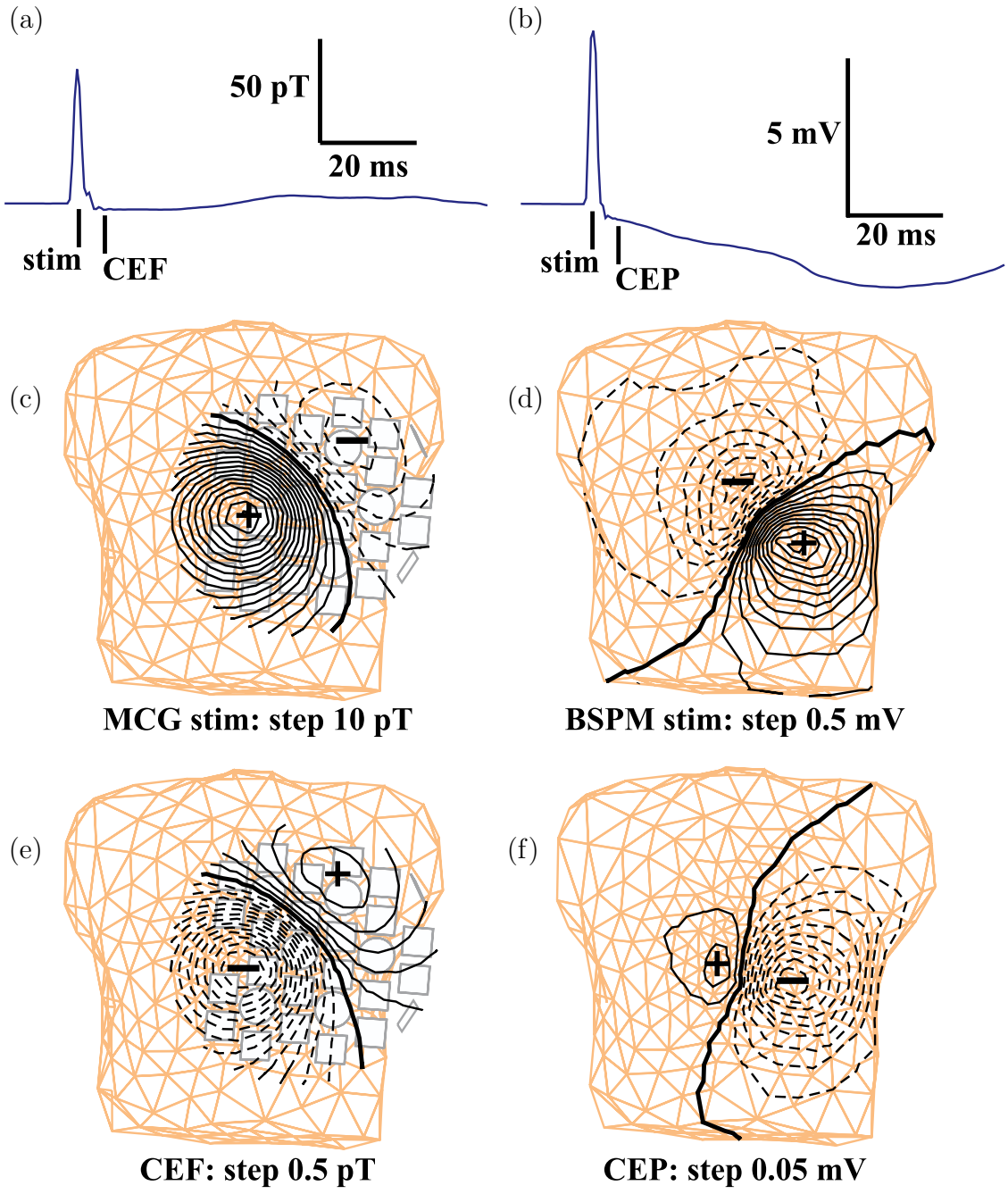

Fig. 5: *a) An MCG signal of a 2–ms pacing stimulus followed by a cardiac evoked field (CEF). b) A simultaneously recorded BSPM signal of the stimulus spike followed by a cardiac evoked potential (CEP). c) The distribution of the magnetic field perpendicular to the dewar bottom, and d) the electric potential on the surface of the torso during the stimulus peak. The isocontour lines in the beginning of e) CEF and f) CEP. (From Publication III)*

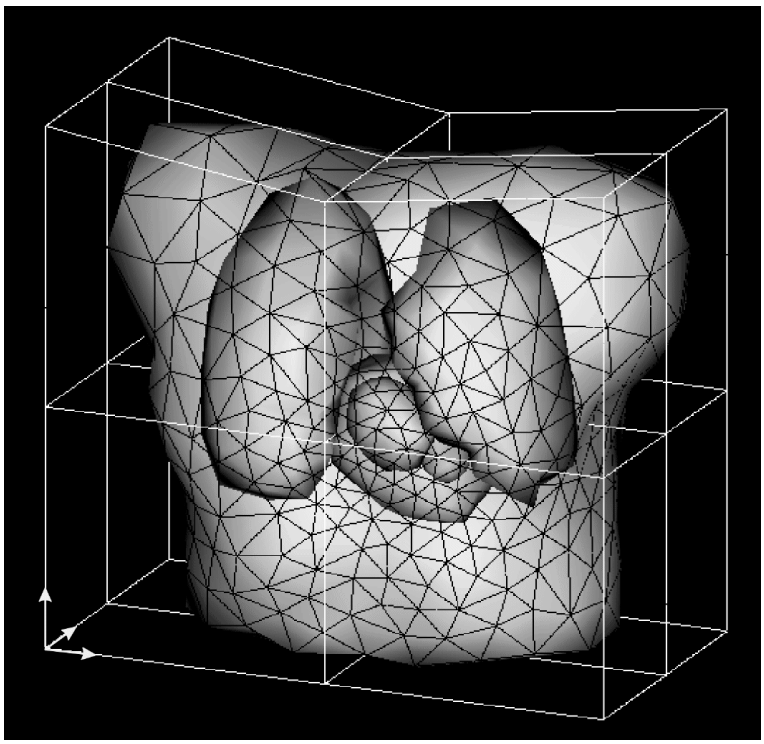

Fig. 6: *Elastic deformation of a reference torso model using a deformation grid. In this case, both shoulders were raised by 3 cm from their original positions, thus simulating the positioning differences during the MRI and the MCG measurements. (From Publication IV)*

the effect of the torso model on the MCG and BSPM dipole localization accuracies. They included an anisotropic skeletal muscle layer in the torso model in an approximative manner and found that the potential on the body surface was smoothed by the anisotropic layer. This lead to overestimation of the source depth which was more pronounced in the electric than in the magnetic case. Hren *et al* (1996) used an inhomogeneous BE model in the forward computations and discovered that removing the inhomogeneities from the torso model affected the BSPM localizations slightly less than the MCG localizations. Hren *et al* (1998) localized pre–excitation sites along the AV ring from simulated MCG and BSPM data, and found that using a homogeneous BE model in the inverse calculations caused average localization errors of 10–15 mm both from the MCG and BSPM data.

In Publication IV, the changes in magnetocardiographic ECD localization results were evaluated when the geometry and the topology of BE torso models were altered. Individual thorax models of three patients were built using the segmentation and triangulation methods developed earlier (Lötjönen *et al* 1998, Lötjönen *et al* 1999a). These torso models were serving as reference models which included the surfaces of the torso, the heart, the lungs and the cavities. Thereafter, the reference models were modified to represent different aspects of the BE model generation process. The resulting changes in the localizations were defined

by computing the distances from the ECD localizations obtained with the reference models to the ECD localizations produced by the variated models. Both simulated and measured multichannel MCG data were used in the calculations. The results showed that the effect of inhomogeneities (lungs, intraventricular blood) was significant for deep source locations. However, superficial sources could be localized within a few millimeters even with non–individual, so–called standard torso models. In general, the thorax model should extend long enough in the pelvic region, and the positions of the lungs and the ventricles should be known in order to obtain accurate localizations. An example of an elastic modification of a reference model used in Publication IV is presented in Fig. 6. The modification was performed with a deformation grid which allowed, e.g., a realistic simulation of the differences in the positions of the shoulders during the MR imaging with respect to the MCG recordings.

4 Equivalent current density

Magnetocardiographic inverse studies with point–like source models, such as the ECD, are generally applicable only for sources confined in a small volume of tissue, e.g., at the onset of the ventricular depolarization. After the onset, the electrical activation spreads in the myocardium as a wavefront, and the use of point–like source models can no longer be physiologically justified. Therefore, distributed source models provide a more general description of the current sources in the heart. In the following, the calculation of a distributed current density, especially applied in biomagnetic inverse studies, will be presented. This source model consists of dipolar elements with fixed locations. Other distributed source models used in solving the cardiac inverse problem are the previously mentioned epicardial and transmembrane potential distributions.

In the literature, the calculation of the equivalent current density was first formulated by Hämäläinen and Ilmoniemi (1984). The calculation of the dipole amplitudes and directions was based on minimum norm estimation, and the solution was called the *minimum norm estimate* (MNE). Consequently, various methods for altering the nature of the solution have been presented in the literature. In this thesis, the solutions of the cardiomagnetic inverse problem, approximating the primary current distribution with dipolar elements, are called minimum norm estimates, or more generally, *current density estimates* (CDEs).

Solving the inverse problem with a distributed source model, such as the CDE, leads to an *ill–posed* problem. The ill–posedness is a mathematical reflection of physical phenomena that include the attenuation and smoothing effects of the volume conductor, and the measurement noise. Rapid spatial variations in the current distribution inside the heart are blurred and smoothed in the measured magnetic or electric data. Therefore, a small amount of perturbation (noise, errors in the volume conductor model, discretization effects etc.) in the MCG or ECG data tends to be magnified in the inverse solution. The calculation can be stabilized by using *regularization*. The regularization produces solutions which may "fit" worse to the data than the original, unregularized solution but usually are more realistic and stable. Different regularization schemes applicable in the cardiac inverse problem have been investigated especially with the epicardial potential distribution (e.g., Messinger–Rapport and Rudy 1988, Oster and Rudy 1992, Oster and Rudy 1997, Ahmad *et al* 1998, Brooks *et al* 1999), and many of the methods can also be used in calculating CDEs.

4.1 Lead fields

The measured magnetic field values and the primary current distribution can be linked together via the *lead fields* $\mathbf{L}_i$ (Baule and McFee 1970)

$$B_i(\mathbf{r}_i) = \int_{V'} \mathbf{L}_i(\mathbf{r}\,') \cdot \mathbf{J_p}(\mathbf{r}\,')\; dv' \;, \tag{20}$$

where $\mathbf{r}_i$ is the location and B_i the magnetic signal detected by the i^{th} sensor. In the discretization of the problem, the source volume V' is replaced by a finite set of source points $\mathbf{r}'_k$. Thereafter, the sensor lead fields are calculated by placing unit dipoles in x–, y– and z–directions to each source point $\mathbf{r}'_k$. In the calculation of the lead fields, the properties of the volume conductor are taken into account. Discretization of Eq. 20 produces a matrix equation

$$\mathbf{B} = L\mathbf{J} \ , \tag{21}$$

where vector $\mathbf{B}_{m\times 1}$ contains the magnetic field values, matrix $L_{m\times 3n} = (\mathbf{L}_1, \cdots, \mathbf{L}_m)$ is composed of the lead fields, and vector $\mathbf{J}_{3n\times 1} = (J_{1x}, J_{1y}, J_{1z}, J_{2x}, \cdots, J_{nz})^T$ contains the unknown source strengths. The number of observations (sensors) is m while n is the number of source points. The conventional minimum norm solution of an under–deterministic matrix equation, such as Eq. 21, can be expressed as

$$\mathbf{J} = L^{\dagger}\mathbf{B} = L^T(LL^T)^{-1}\mathbf{B} \ , \tag{22}$$

where $L^{\dagger}$ is the pseudo–inverse of L. Eq. 22 relates directly to solution $\mathbf{J}^*$ presented by Hämäläinen and Ilmoniemi (1984, 1994), which is defined as a linear combination of the lead fields

$$\mathbf{J}^* = \sum_{i=1}^{m} \omega_i \mathbf{L}_i = \boldsymbol{\omega}^T L \ . \tag{23}$$

The coefficients ω_i in Eq. 23 are solved from the magnetic field values using the inner product matrix Γ ($\Gamma_{ij} = \langle \mathbf{L}_i, \mathbf{L}_j \rangle$):

$$\boldsymbol{\omega} = \Gamma^{-1}\mathbf{B} = (LL^T)^{-1}\mathbf{B} \ . \tag{24}$$

Therefore, the transpose of $\mathbf{J}^*$ equals to the solution in Eq. 22.

In practice, the unknown source strengths $\mathbf{J}$ cannot be directly solved from Eq. 22 because the lead fields of adjacent sensors are nearly linearly dependent on each other. Therefore, the inner product matrix (LL^T) has a low numerical rank, and the classical solution will be contaminated by noise. The calculation can be stabilized by using regularization.

4.2 Regularization

In the literature, the truncation of the singular value decomposition (tSVD) (Hämäläinen and Ilmoniemi 1994, Nenonen *et al* 1994), Tikhonov regularization (e.g., Ferguson and Stroink 1995a) and Wiener regularization (Numminen *et al* 1995) have been used in stabilizing the calculation of the current density estimates. In addition, different iterative, temporal and statistical regularization methods, mostly related to the calculation of the epicardial potential distribution, have been presented. In the following, these methods are briefly reviewed.

4.2.1 Truncated SVD

In tSVD regularization, a singular value decomposition is first performed for the inner product matrix Γ so that $\Gamma = UDU^T$, where U is orthonormal and D is a diagonal matrix, containing the singular values d_i. The matrix inverse can be obtained from $\Gamma^{-1} = UD^{-1}U^T$, where $D^{-1} = \mathrm{diag}(d_1^{-1}, \cdots, d_m^{-1})$. The truncation of the singular values is performed by replacing D^{-1} with $\mathrm{diag}(d_1^{-1}, \cdots, d_k^{-1}, 0, \cdots, 0)$. Replacing the last $m - k$ diagonal elements by zeroes stabilizes the inversion because the smallest singular values are mainly associated with noise and cause large numerical errors in the matrix inversion. The truncation index k should be selected so that the noise of the data minimally affects the solution.

4.2.2 Tikhonov regularization

In Tikhonov regularization (Tikhonov and Arsenin 1977), a compromise is sought between a solution that matches the data but may be unrealistic and unstable, on one hand, and the fulfillment of a side constraint based on *a priori* knowledge (or assumption) about a realistic and stable solution, on the other. The general form of the function to be minimized can be expressed as

$$\|L\mathbf{J} - \mathbf{B}\|^2 + \lambda\|R(\mathbf{J} - \mathbf{J}^+)\|^2 \longrightarrow \min\,, \tag{25}$$

where $\|\cdot\|$ is the Euclidean norm, R is the regularization operator, λ is a parameter which controls the weight given to the minimization of the side constraint, and $\mathbf{J}^+$ is an *a priori* estimate for the solution $\mathbf{J}$. The use of a side constraint changes the classical solution towards the applied side constraint. If a reasonable $\mathbf{J}^+$ is not available, it is usually discarded from the calculations. Thereafter, the solution to the minimization problem in Eq. 25 can be written as

$$\mathbf{J} = L_{\mathrm{reg}}\mathbf{B} = (L^TL + \lambda R^TR)^{-1}L^T\mathbf{B}\,, \tag{26}$$

or alternatively

$$\mathbf{J} = (R^TR)^{-1}L^T(L(R^TR)^{-1}L^T + \lambda I)^{-1}\mathbf{B}\,, \tag{27}$$

provided that the regularization operator R has a full rank $3n$. Both solutions involve the inversion of a $3n \times 3n$ matrix, therefore increasing the computational demands with an increasing number of source points.

Regularization operator The regularization operator R can be implemented in several ways. The use of the identity matrix I tends to minimize the norm of the solution, or more generally, the norm of the difference between the solution and the *a priori*. In that case, Eq. 27 reduces to $\mathbf{J} = L^T(LL^T + \lambda I)^{-1}\mathbf{B}$, which involves the inversion of an $m \times m$ matrix only, and is therefore quickly computed.

Discrete approximations of derivative operators (difference, Laplacian) used as the regularization operator tend to reduce either steepness or steep changes in the solution. The

discrete surface Laplacian operator Δ can be constructed, e.g., by using one of the approximations presented by Huiskamp (1991). In the simplest approximation, the Laplacian of a general function f is formulated for a regular plane grid:

$$\Delta f_0 \approx C \sum_{i=1}^{N} (f_i - f_0) \ , \tag{28}$$

where f_0 is the value of the function in the central point, f_i are the values in the N neighboring grid points, and C is a constant depending on N and on the distance between the central and the neighboring points. In a regular grid, the neighboring points are spaced at equal angles with a constant distance from the central point. Therefore, Eq. 28 is valid, e.g., for a grid consisting of equilateral triangles. In a more general case, such as on the triangulated surface of the heart, the distances and the spacing angles of the neighboring grid points need to be taken into account in the Laplacian. However, the crude approximation given by Eq. 28 has been found to be sufficient with respect to a more accurate formulation in the regularization of uniform double layer solutions on the ventricular surface (Huiskamp 1991).

In Publication VI, realistic surfaces of the torso and the left ventricle (LV) were used to test the zero– and second–order regularization of CDEs calculated from simulated, distributed current sources located on the surface of the LV. The simulated MCG data also contained a realistic amount of measurement noise. For deeper source locations, the zero–order regularization was found to shift the estimates towards the anterior surface of the LV. With second–order regularization, the estimates were correctly centered with respect to the known source region. An example of the comparison between the regularization operators, carried out for a deep source location, is presented in Fig. 7.

Selecting a value for λ In the literature, numerous methods have been presented for selecting a proper value for the regularization parameter λ. These methods include, e.g., the discrepancy technique (Morozov 1984), the generalized cross–validation (Golub *et al* 1979), and the L–curve method (Hansen 1992). More recently, a technique based on zero–crossing of the function in Eq. 25 has been presented (Johnston and Gulrajani 1997). The L–curve method, also applied in this thesis, has been most widely used in the regularization of the biomagnetic inverse problem.

A numerical algorithm to compute an optimal value of λ by using the L–curve method has been presented by Hansen and O'Leary (1993). With the L–curve, a balance between the minimization of the residual and the side constraint in Eq. 25 can be found as the value of λ is varied. The name of the method relates to the shape of a continuous curve $C_0 : \{\|L\mathbf{J} - \mathbf{B}\|, \|R\mathbf{J}\|\}$. In the over–determined case of solving the epicardial potential distribution from body surface potentials, the L–curve method has been formulated by Clements *et al* (1994). By using the generalized singular value decomposition of the matrices $L = UCX^{-1}$ and $R = VSX^{-1}$, the regularizing matrix L_{reg} in Eq. 26 can be written as $X(C^TC + \lambda S^TS)^{-1}C^TU^T$

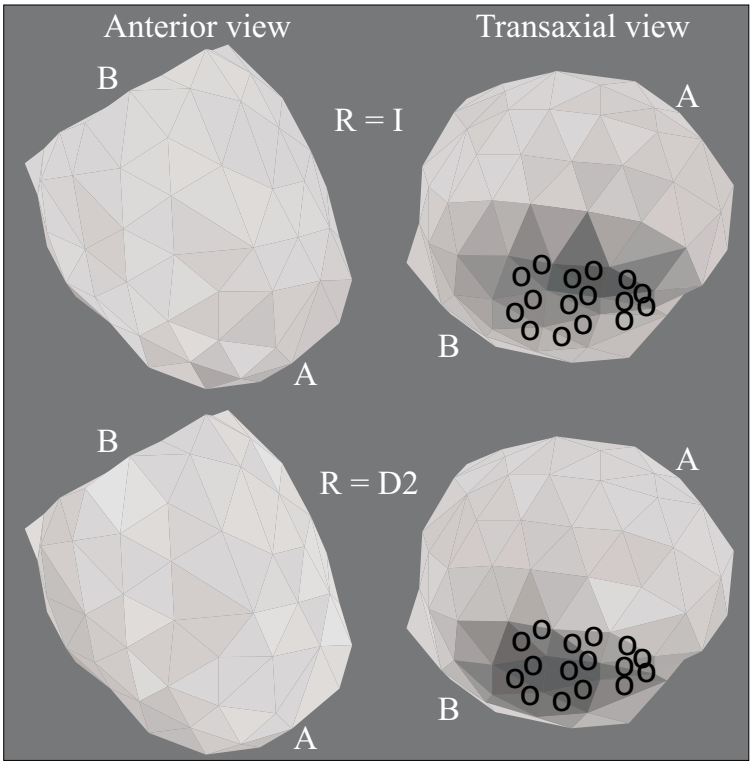

Fig. 7: *CDEs calculated for a distributed current source, located on the posterior surface of the LV, using zero–order (upper row) and second–order (bottom row) Tikhonov regularization. The actual positions of the dipoles used in generating the data are marked with black circles. The amplitude of CDEs is coded with grayscale values; darkest gray indicates largest current density (A = apex, B = base). (From Publication VI)*

(Clements *et al* 1994). In the decomposition, U and V are orthonormal, and X is non–singular. If L is assumed to have full rank m and R is assumed to have full rank $3n$, the matrices C and S for the under–deterministic case in Eq. 21 are of the form

$$C = \begin{pmatrix} O_{m\times(3n-m)} & C_m \end{pmatrix} , \qquad S = \begin{pmatrix} I_{3n-m} & O_{(3n-m)\times m} \\ O_{m\times(3n-m)} & S_m \end{pmatrix} ,$$

where $C_m = \mathrm{diag}(\alpha_1, \cdots, \alpha_m)$ and $S_m = \mathrm{diag}(\beta_1, \cdots, \beta_m)$. The generalized singular values of matrices L and R are defined as $\mu_i = \frac{\alpha_i}{\beta_i}$. Therefore, the regularized solution $\mathbf{J}$ in Eq. 26 can be expressed as

$$\mathbf{J} = \sum_{i=1}^{m} \frac{1}{\beta_i} \frac{\mu_i}{\mu_i^2 + \lambda} \langle \mathbf{u}_i, \mathbf{B} \rangle \, \mathbf{x}_{3n-m+i} , \tag{29}$$

where $\mathbf{u}_i$ refers to the i^{th} column of U and $\mathbf{x}_{3n-m+i}$ to the $(3n-m+i)^{th}$ column of X. By using the expression in Eq. 29, the squared norm of the residual can be written as

$$\|L\mathbf{J} - \mathbf{B}\|^2 = \sum_{i=1}^{m} \left[\frac{\lambda}{\mu_i^2 + \lambda} \langle \mathbf{u}_i, \mathbf{B} \rangle \right]^2 , \tag{30}$$

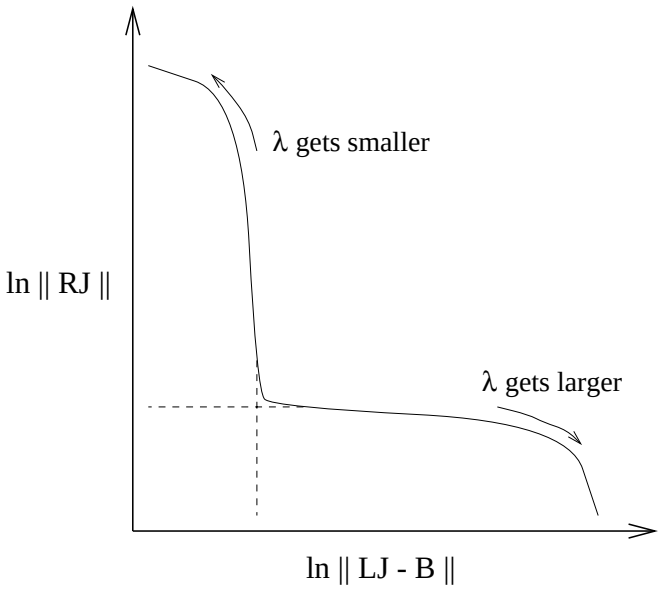

Fig. 8: *A schematic presentation of the shape of the L–curve.*

and the squared norm of the side constraint is

$$\|R\mathbf{J}\|^2 = \sum_{i=1}^{m} \left[\frac{\mu_i}{\mu_i^2 + \lambda} \langle \mathbf{u}_i, \mathbf{B} \rangle \right]^2 . \tag{31}$$

Eqs. 30 and 31 again coincide with the results presented by Clements *et al* (1994). It can be seen that as the value of λ is increased, the norm of the residual is increasing while the norm of the side constraint is decreasing. The opposite is true for decreasing λ values.

The L–curve is usually plotted on a log–log scale. By defining the functions $x(\lambda)$ and $y(\lambda)$ as

$$x(\lambda) = \frac{1}{2} \ln \left(\sum_{i=1}^{m} \left[\frac{\lambda}{\mu_i^2 + \lambda} \langle \mathbf{u}_i, \mathbf{B} \rangle \right]^2 \right) , \tag{32}$$

$$y(\lambda) = \frac{1}{2} \ln \left(\sum_{i=1}^{m} \left[\frac{\mu_i}{\mu_i^2 + \lambda} \langle \mathbf{u}_i, \mathbf{B} \rangle \right]^2 \right) , \tag{33}$$

the value of the residual can be plotted as a function of the side constraint with varying λ. A schematic illustration of the shape of the curve is presented in Fig. 8. The goal is to find a value for λ which balances the minimization between the residual and the side constraint at the "corner" point of the L–curve. The corner is defined to have a maximal curvature. A mathematical expression for the curvature can be obtained from

$$\kappa(\lambda) = \frac{x'(\lambda)y''(\lambda) - y'(\lambda)x''(\lambda)}{((x'(\lambda))^2 + (y'(\lambda))^2)^{3/2}} . \tag{34}$$

The first and second order derivatives of functions $x(\lambda)$ and $y(\lambda)$ with respect to λ have been formulated in Publication V in the case $R = I$. However, the formulations also hold for a

more general choice of R if the singular values in the formulas of Publication V are replaced with the generalized singular values μ_i.

For the existence of the corner point of the L–curve, Hansen (1992) has presented conditions which include, e.g., that the noise in the measured data is randomly distributed and has a zero mean, and that the amplitude of the noise is smaller than the amplitude of the signal. Especially the former condition might not be satisfied because correlated noise can be present in the measured data. Also the reduction of the signal amplitude tends to distort the shape of the L–curve. Therefore with measured data, the curvature function given in Eq. 34 sometimes results in multiple maxima, and the corner point cannot be uniquely defined. However, a reasonable value for λ can be obtained by inspecting the quality of the calculated CDEs.

4.3 Weighted solutions

A scheme for weighting, or pre–conditioning of the lead field matrix has been proposed by Ferguson *et al* (1995b) by adding a diagonal matrix D into the original matrix formulation of Eq. 21:

$$\mathbf{B} = LDD^{-1}\mathbf{J} \ . \tag{35}$$

Thus, the original equation does not change due to the addition of the weighting matrix D. In D, possible *a priori* information about the solution can be used. If the product of matrices L and D is denoted as $\tilde{L}$, the solution of the under–determined Eq. 35 can be written as (Ferguson *et al* 1995b)

$$\mathbf{J} = D[\tilde{L}^T(\tilde{L}\tilde{L}^T)^{-1}\mathbf{B}] \ . \tag{36}$$

Although the original equation does not change due to the addition of the weighting matrix, the solution of Eq. 36 changes. Ferguson *et al* (1995b) proposed the matrix D to be diagonal, and the diagonal elements to equal to the square roots of the best–fitting dipole strength at each of the source locations. They found that with simulated data, the pre–conditioning of the lead field matrix improved the quality of the solutions with respect to the tSVD and Tikhonov regularized solutions. The pre–conditioning tends to favor deeper solutions as the weights for deeper sources will be larger than those of the shallow sources. Despite the addition of the weighting matrix D, the matrix to be inverted in Eq. 36 is close to singular. The truncation of the SVD or Tikhonov regularization can be used in balancing the computation of the weighted solutions.

The weighting of the solution can also be applied iteratively. A method for iterative weighting, termed as the FOCUSS algorithm, was suggested by Gorodnitsky *et al* (1995). In this approach, the elements of the weighting matrix D are updated using the information obtained during previous iterations. Gorodnitsky *et al* (1995) suggested to initialize D with the identity matrix. In the following iterations, they proposed that the elements of D would

be obtained from the components of the current distribution calculated during the previous iterations:

$$D^k = \begin{pmatrix} J_{1,x}^{k-1} & & 0 \\ & \ddots & \\ 0 & & J_{n,z}^{k-1} \end{pmatrix}, \tag{37}$$

where $J_{i,j}^{k-1}$ is the j^{th} component of a dipole located in the i^{th} source point calculated during the $k-1^{th}$ iteration. Alternatively, information about all the previous solutions can be added to the weighting matrix:

$$D^k = D^{k-1} \cdot \begin{pmatrix} J_{1,x}^{k-1} & & 0 \\ & \ddots & \\ 0 & & J_{n,z}^{k-1} \end{pmatrix}. \tag{38}$$

The iterations are continued until the magnitudes of the changes in the solution are below a pre–set limit.

The truncated SVD, the zero–order Tikhonov regularization, the weighting and the iterative weighting approaches were tested in Publication V by using measured MCG data. The weighting matrix D was initialized with the square roots of the optimal dipole strengths. The measurements were carried out with a non–magnetic catheter in the heart, thus providing an exact validation for the location of the current source. It was found that when the source was located relatively close to the sensors, all regularization techniques were able to localize the center point of the source region. However, for a deeper source location, weighting was required to produce a correct estimate of the underlying current distribution.

Another iterative approach has been suggested by Tilg *et al* (1995) where the number of the reconstruction points was reduced by removing the point with the smallest dipole amplitude in the subsequent step of iteration. The iterations were terminated at a prescribed number of source points. The method was found to localize both focal and distributed sources from simulated MCG data. However, the number of the source points to be included in the final solution might be difficult to determine with measured MCG data (Tilg *et al* 1995).

4.4 Temporal and statistical regularization

In addition to the one time point –approach described above, temporal information can be used in the regularization process. This has been proposed, e.g., by Oster and Rudy (1992) who found a marked improvement in the inversively reconstructed epicardial potential distribution when information from previous time instants were incorporated in the calculation. Spatial characteristics of the measured data can also be taken into account. Oster and Rudy (1997) suggested a regional regularization approach in reconstructing the epicardial potential distribution. In their method, the amount of regularization was adjusted according to the spatial characteristics of body surface potential maps. The method was found to improve the epicardial potential reconstruction with respect to global regularization where the

amount of regularization was controlled with one parameter only. In addition, Brooks *et al* (1999) used multiple constraints (both spatial and temporal) in Tikhonov–type regularization and presented a so–called L–surface method for selecting values for the regularization parameters.

Among the statistical regularization schemes proposed, the incorporation of the spatial covariance in solving the epicardial potential distribution was first suggested by Martin *et al* (1975). Recently, the method has been studied by van Oosterom (1999). In this approach, the solution is formulated as the *maximum–a–posteriori* estimate which incorporates the spatial covariances of the epicardial potential distribution and the noise. Van Oosterom (1999) found that the inverse solution was more robust with respect to perturbations (noise, inhomogeneities) than the solutions obtained with zero– and second–order Tikhonov regularization. Sekihara and Scholz (1996) used a generalized Wiener estimation technique and found that the method could reconstruct 3D current distributions in case of simulated data.

4.5 Applications of CDE

4.5.1 Ischemia studies

One of the most interesting areas in clinical MCG today is the detection and characterization of myocardial ischemia and viability. A new and accurate non–invasive method for recognition of ischemia would have important clinical applications, especially because novel therapeutic interventions for revascularization (e.g., coronary angioplasty and transmyocardial laser) are emerging. An acute ischemia changes the shape of the action potential of myocardial cells. The mechanisms causing the changes have been investigated, e.g., by Shaw and Rudy (1997a, 1997b). Typically, the value of the resting potential is increased in ischemic cardiac cells, whereas during the plateau phase (see Fig. 1) the value of the membrane potential is decreased with respect to the monophasic action potential of a healthy cell. Such changes lead to an *injury current* which in the resting state flows from the ischemic area into the healthy myocardium, and in the opposite direction during the repolarization. In MCG recordings, the ischemia reflects as changes (elevations or depressions) during the ST–segment (e.g., Cohen *et al* 1971, 1983, and Savard *et al* 1983).

Infarcted and ischemic regions have been simulated, e.g., by Czapski *et al* (1998) who compared the isocontour maps of anterior and inferior myocardial infarction (MI) to the ones produced by a healthy heart. They found that the isocontours of the difference maps more or less maintained their pattern throughout the depolarization. To investigate the applicability of the CDE in localizing ischemia from MCG measurements, Killmann *et al* (1995) used a computer model of the human heart to simulate the excitation and repolarization processes in different cases of myocardial ischemia. The CDE was applied at the S–point of the QRS–complex in a plane positioned 7–10 cm below the simulated MCG measurement grid. The

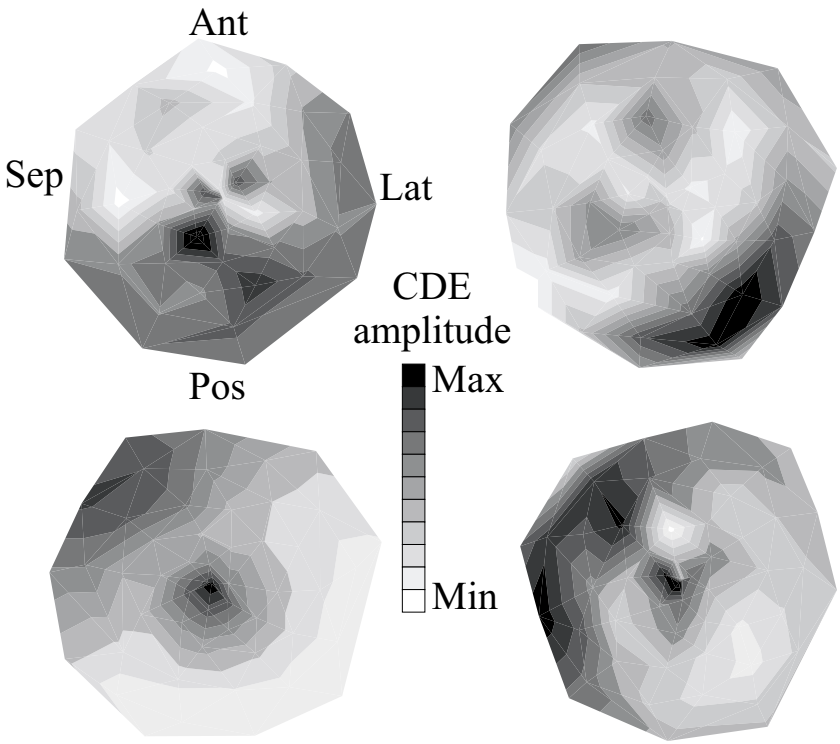

Fig. 9: *CDEs for two RCA patients (upper row) and for two LAD patients (bottom row), visualized with polar maps (Ant = anterior, Lat = lateral, Pos = posterior, and Sep = septal region). The amplitudes of the CDEs for each patient are coded with grayscale values. (From Publication VI)*

direction of the dipolar elements in CDE and the position of the largest elements were found to reflect the location of the ischemic area.

In Publication VI, CDE was applied on the epicardial surface of the LV in 13 CAD patients. In the MCG measurements, exercise testing was used as described by Takala (1999) to induce acute ischemia in the cardiac tissue. The individual torso and LV surfaces were constructed from MR images. The current density estimates were calculated from the ST–segment exercise–rest difference signals using second–order Tikhonov regularization. The calculated CDEs were compared to the clinical reference information about the LV function. In four patients with a single–vessel CAD, an increase in the CDE amplitude was found to correlate with the expected ischemic myocardial regions, supplied by the stenotic coronary artery. The CDEs of the single–vessel CAD patients are shown in Fig. 9 as polar map presentations. In the polar maps, the apex of the heart is projected at the center. The map can roughly be divided into four regions according to the coronary anatomy: anterior, lateral, posterior, and septal regions. In the two patients with a stenosis in the right coronary artery (RCA), an increase in the CDE amplitude is detected in the posterior region of the LV which corresponds to the expected ischemic myocardial regions in patients with a stenosis in the RCA. In the two patients with a stenosis in the left anterior descending (LAD) coronary

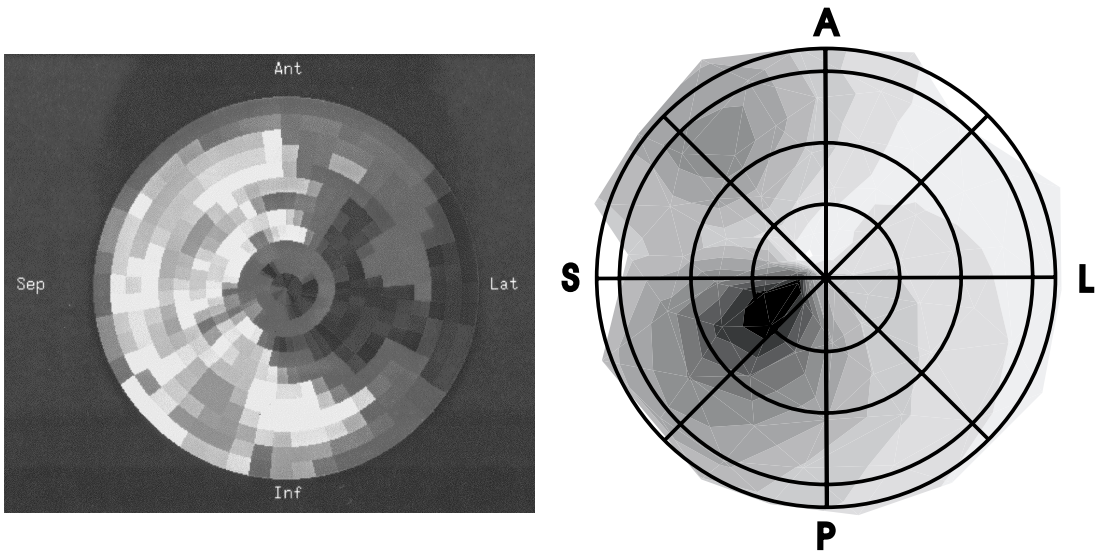

(a) (b)

Fig. 10: *a) The PET result of a three–vessel CAD patient showing a scar in the lateral region (dark area). b) The CDE corresponding to the PET result in (a) together with the division of the polar map into 24 segments. The darkest gray indicates highest CDE amplitude. (From Publication VI)*

artery, the CDEs are focused in the apex, in the anterior and in the septal regions of the LV, thus matching to the myocardial regions supplied by the LAD.

Nine of the patients in Publication VI had three–vessel CAD with regional or global LV dysfunction caused by severe chronic myocardial ischemia, previous MI or both. In this patient group, positron emission tomography (PET) images were used to separate the areas of viable myocardial tissue from the scar regions. Also in this patient group, the CDEs were calculated from the ST–segment exercise–rest difference signals. The analysis of the CDEs was based on the fact that no current should build up in MI scar regions. The calculated CDEs were compared to the PET data by dividing the polar map of the LV into eight sectors: two anterior, two lateral, two septal, and two posterior sectors. Each sector was further divided into three short axis planes: apex, middle, and base. Thus, the comparison was carried out in 24 segments which, by PET, were determined to be either viable tissue or scar. The scale of the CDEs was divided to indicate low and high CDE amplitude. Therefore, a match was obtained if a low CDE amplitude was detected in a scar segment, or a high CDE amplitude in a viable segment.

An example of the comparison between PET and CDE carried out in Publication VI is presented in Fig. 10. The PET result indicates a lateral scar area which is shown as a dark region. The anteroseptal, septal and posteroseptal regions indicate viable myocardium. The corresponding CDE shows an increased amplitude in the anteroseptal, septal and posteroseptal regions, thus matching well with the PET data. A decreased CDE amplitude is

observed in the lateral region which was found to be a scar area.

The overall results of the comparison between PET data and calculated CDEs for all nine three–vessel CAD patients showed an average match of 77 % between the segments of high and low amplitude in CDEs, and the viable and scar areas in PET, respectively. Therefore, the classification (scar or viable tissue) obtained from the calculated CDEs was correct in approximately 18/24 segments. In Publication VI, the CDE was thus found to be a potential method for localizing both myocardial ischemia in single–vessel CAD patients, as well as more complex forms of ischemia in three–vessel CAD patients.

In addition to MCG studies, ischemic regions have also been localized from multichannel BSPM measurements by solving the epicardial potential distribution (MacLeod *et al* 1995). In this study, seven patients underwent percutaneous transluminal coronary angioplasty (PTCA) where the balloon inflations produced acute transient ischemia. The estimated ischemic regions, determined from the calculated epicardial potential distributions, were compared to a qualitative estimate of the perfusion region based on fluoroscopic examination of each patient's coronary anatomy and PTCA balloon location. It was found that the ischemic regions, predicted by the epicardial potential distributions, included the perfusion zone determined fluoroscopically.

4.5.2 Other clinical studies

The CDE was applied by Leder *et al* (1998) in two MI patients and in two healthy subjects. Current density estimates were calculated on the surface of the left ventricle during ventricular depolarization to detect a decreased current amplitude in the MI patients. Low regional and global current densities were found in the MI patients. Regions of low current density were found to correspond to infarcted segments. The CDEs of the healthy subjects displayed less marked areas of low current density.

The origin site of a malignant ventricular tachycardia (VT) has also been localized with current density estimation (Müller *et al* 1999). The CDE was calculated on the surface of the left ventricle. The origin site of the VT, determined from the X–ray images of the ablation catheter position during EP studies, was used as the gold standard. The area with the highest current density in the CDE was then compared to the gold standard. It was found that the CDE localized the origin of the VT within 10 mm.

5 Uniform double layer

The activation sequence on the ventricular surface, including both epi– and endocardium, can be estimated from BSPM and/or MCG data with the uniform double layer (UDL) source model. This spatio–temporal model consists of elementary double layer current sources of equal strength. The direction of the double layer sources is perpendicular to the surface, and they are oriented inwards in the cardiac muscle. The parameters of the model are the activation times of each double layer element during the ventricular depolarization phase. The justification of the model can be derived from the bidomain model in the sense that if equal anisotropy ratios in the intra– and extracellular domains are assumed, the volume distribution of cardiac sources can be replaced by an appropriate double layer on the surface of the heart. Calculation methods required in finding an UDL based inverse solution have been developed, e.g., at the University of Nijmegen in the Netherlands (Huiskamp and van Oosterom 1988). Previously, UDL based inverse solutions have been calculated mainly from BSPM recordings. Solving the cardiac inverse problem with the UDL model has been found to be less ill–posed than using the epicardial potential distribution as the source model, and very promising results have been obtained (e.g., Tilg *et al* 1997). However, until recently, the quality of UDL based inverse solutions has been evaluated with invasive data only in a small number of situations. In this thesis, invasively recorded epicardial potential data were used as a reference in estimating the quality of epicardial activation times calculated from both BSPM and MCG recordings.

5.1 Formulation of the UDL model

In the UDL model, the magnetic field or the electric potential is considered to be generated by double layer (dipolar) current source elements located on the ventricular surface S'. The mapping between the current source elements and the field values is described by a (magnetic or electric) transfer function $A(\mathbf{r}, \mathbf{r}\,')$ and by the ventricular activation times $\tau(\mathbf{r}\,')$. Once the activation wavefront has reached the point $\mathbf{r}\,'$ (at time $\tau(\mathbf{r}\,')$), the point remains activated throughout the whole depolarization sequence. The basic equation for the UDL model is

$$F(\mathbf{r}, t) = \int_{S'} A(\mathbf{r}, \mathbf{r}\,') H(t - \tau(\mathbf{r}\,'))\; dS' \tag{39}$$

where $F(\mathbf{r}, t)$ denotes either to the measured component of the magnetic field or to the electric potential in point $\mathbf{r}$ at time t. $H(t - \tau(\mathbf{r}\,'))$ is the Heaviside step function accounting for the fact that the elementary source at $\mathbf{r}\,'$, once switched on at time $\tau(\mathbf{r}\,')$, remains on until the whole ventricular surface S' has been activated (Huiskamp and van Oosterom 1988).

The inverse problem now consists of finding the unknown activation times $\tau(\mathbf{r}\,')$ in the activation time interval $[0, T]$ when the magnetic field or potential values $F(\mathbf{r}, t)$ on the measuring surface S are known. The activation times can be obtained by solving the following

minimization problem:

$$\int_0^T \int_S \left(\int_{S'} A(\mathbf{r}, \mathbf{r}\,')H(t - \tau(\mathbf{r}\,'))\ dS' - F(\mathbf{r}, t) \right)^2 dS\ dt \longrightarrow \min\ . \tag{40}$$

In the discretization of Eqs. 39 and 40, the finite extent of the elementary sources on the ventricular surface needs to be taken into account. This can be achieved by smoothing the Heaviside step function $H(t - \tau(\mathbf{r}\,'))$ in a suitable way (Huiskamp and van Oosterom 1988). Solving the activation times is also an ill–posed problem in the sense that small changes in $F(\mathbf{r}, t)$ may cause large variations in $\tau(\mathbf{r}\,')$. Therefore, regularization methods are again needed to stabilize the calculation. Within the UDL model, Tikhonov regularization with the surface Laplacian (Huiskamp 1991) as the regularization operator R is usually used, because it can be assumed that there are no sudden changes in the activation times of adjacent points on the ventricular surface. The discretized and regularized minimization problem related to Eq. 40 then states:

$$\|A\Upsilon^w_{\boldsymbol{\tau}} - F\|^2 + \lambda \|R\boldsymbol{\tau}\|^2 \longrightarrow \min\ , \tag{41}$$

where $\Upsilon^w_{\boldsymbol{\tau}}$ contains the smoothed activation times $\boldsymbol{\tau}$. The smoothing of the Heaviside step function is controlled with the parameter w (Huiskamp and van Oosterom 1988) while the amount of regularization is again controlled with the parameter λ.

The minimization of Eq. 41 is carried out with a quasi–Newton optimization algorithm, which iteratively finds better solutions $\boldsymbol{\tau}$ that minimize Eq. 41. In the algorithm, an initial estimate for the activation times is needed. The quality of the initial estimate should be as high as possible in order to prevent the minimization algorithm from converging into local minima. There are at least two ways of calculating the initial estimate. In the first approach, an integration over the QRS–complex is performed for Eq. 39:

$$\int_0^T F(\mathbf{r}, t)\ dt = \int_0^T \left[\int_{S'} A(\mathbf{r}, \mathbf{r}\,')H(t - \tau(\mathbf{r}\,'))\ dS' \right]\ dt\ , \tag{42}$$

where the left–hand side can be reduced into the summation of the magnetic field or the potential values at the observation point $\mathbf{r}$, and the right–hand side effectively contains the values of the transfer matrix A multiplied by the activation times $\boldsymbol{\tau}$. With the definition $f(\mathbf{r}) \equiv \int_0^T F(\mathbf{r}, t)\ dt$, a discretized version of Eq. 42 can be expressed as

$$\boldsymbol{f} = A\boldsymbol{\tau}\ . \tag{43}$$

The initial estimate for $\boldsymbol{\tau}$ is then obtained by multiplying the integrated (summed) field values $\mathbf{f}$ with the (regularized) pseudoinverse of A. In the regularization, truncated SVD was applied by Huiskamp and van Oosterom (1988).

In a more recent approach for calculating the initial estimate for $\boldsymbol{\tau}$, Huiskamp and Greensite (1997) used the so–called critical point theorem. In the method, the SVD of the signal matrix F is first calculated: $F = UDV^T$ where U and V are orthonormal matrices. The

matrix D is composed of a diagonal matrix, containing the singular values of F, and a zero matrix. In the case of measured data, from a certain rank r_{eff} onward the singular values will be dominated by noise. This rank is considered to be the effective rank of F, which separates the signals generated by the current sources in the heart and the measurement noise. If the rank r_{eff} is known, the first r_{eff} rows of U can be considered to span the spatial signal space. The remaining rows of U are assumed to span the noise space. The rows of V are said to span the temporal signal and noise spaces.

The construction of the spatial signal space is required in the formulation of the critical point theorem. The critical points $\mathbf{r}'_{\mathbf{cr}}$ of the surface activation function τ are its extremal points where $|\nabla\tau(\mathbf{r}'_{\mathbf{cr}})| = 0$. The critical point theorem, formulated by Greensite (1995), states that $\mathbf{r}'_{\mathbf{cr}}$ is a critical point of τ if, and only if, the transfer vector $\mathbf{A}(\cdot, \mathbf{r}'_{\mathbf{cr}})$ associated with this point is contained in the spatial signal space. This theorem can be utilized by gradually constructing the spatial signal space and by calculating the distances between the transfer vectors $\mathbf{A}(\cdot, \mathbf{r}\,')$ and the signal space. Huiskamp and Greensite (1997) defined the following distance function

$$M_0^t(\mathbf{r}\,') = \left| 1 - \sum_{i=1}^{r_{\text{eff}}} \langle \mathbf{a}(\cdot, \mathbf{r}\,'), \mathbf{u}_i \rangle^2 \right|^{-1} , \tag{44}$$

where $\mathbf{a}(\cdot, \mathbf{r}\,') = \mathbf{A}(\cdot, \mathbf{r}\,')/\|\mathbf{A}(\cdot, \mathbf{r}\,')\|$ is the normalized transfer function, $\langle \cdot, \cdot \rangle$ denotes the inner product in the signal space, and $\mathbf{u}_i$ is the i^{th} spatial eigenvector resulting from the SVD of the signal matrix F constrained to the time interval $[0, t]$. The function $M_0^t(\mathbf{r}\,')$ will tend to infinity for a critical point $\mathbf{r}'_{\mathbf{cr}}$ when t reaches the critical time $t_{cr} = \tau(\mathbf{r}'_{\mathbf{cr}})$. Because the separation between the signal and noise spaces is more inaccurate for small values of t than for larger values, Huiskamp and Greensite (1997) introduced two distance functions: $M^+(\mathbf{r}\,', t) \equiv M_0^t(\mathbf{r}\,')$ and $M^-(\mathbf{r}\,', t) \equiv M_t^T(\mathbf{r}\,')$, $0 \leq t \leq T$. The properties of $M^-(\mathbf{r}\,', t)$ will be opposite to $M^+(\mathbf{r}\,', t)$ in the sense that for a critical point, the value of $M^-(\mathbf{r}\,', t)$ will be initially high and experience a sudden drop to a small value at the critical time t_{cr}. Also $M^-(\mathbf{r}\,', t)$ will be more accurate for critical points occurring at early stages of activation.

Finally, the functions $M^+(\mathbf{r}\,', t)$ are $M^-(\mathbf{r}\,', t)$ can be combined into a third function: $Z(\mathbf{r}\,', t) \equiv M^+(\mathbf{r}\,', t) - M^-(\mathbf{r}\,', t)$ which for a critical point will show a zero crossing accompanied by a large positive jump at it's critical time. Huiskamp and Greensite (1997) also found that even for a non–critical point, a zero–crossing in $Z(\mathbf{r}\,', t)$ is observed, although the amplitude of the positive jump is much smaller. As the function $Z(\mathbf{r}\,', t)$ was found to behave like an activation wavefront, an isochrone representation of the zero–crossing times can be made. The reconstructions of zero–crossing times, with correct locations of extremal points, have been used in this thesis as initial estimates for the quasi–Newton algorithm.

5.2 Clinical studies

The UDL model is suitable for describing the ventricular activation which propagates as an activation wavefront in a structurally healthy heart. Huiskamp and van Oosterom (1988) calculated the activation sequences with individual BE torso models for three healthy subjects and compared the results with an experimentally documented ventricular activation sequence (Durrer *et al* 1970). The reference sequence shows initial activation in the left ventricular endocardium, secondary activation in the right ventricular endocardium, early epicardial breakthrough in the anterior part of the right ventricle, and secondary breakthrough in the anterior part of the left ventricle. The latest activation takes place in the posterobasal area of the right ventricle. The activation time maps calculated by Huiskamp and van Oosterom (1988) showed reasonable agreement with the known activation sequence. Oostendorp *et al* (1996) used multichannel MCG and BSPM data recorded in the same patient and calculated the activation times from both datasets. In general, the solutions showed similar features with the root–mean–square (RMS) difference of 6.1 ms. In addition to measured data, Tilg *et al* (1997) also generated simulated MCG and BSPM data for one subject. The relative differences in the activation time maps were 10 % and 15 % for the simulated and measured MCG and BSPM data, respectively.

Until recently, only few validation studies with the UDL model using invasively recorded data have been reported. Huiskamp *et al* (1992) found that the UDL model correctly localized the site of earliest activation from paced BSPM data, obtained from catheterized patients. Oostendorp *et al* (1997) used measured epicardial activation times from a dog heart suspended in a torso shaped tank. In this experiment, the correspondence between the measured and the computed activation times was good, showing an RMS difference of only 4 ms at the epicardial electrodes. In a recent validation study, Tilg *et al* (1999) used invasive human data recorded with an electroanatomical catheter mapping system (CARTO$^{\mathrm{TM}}$, Biosense, Ltd.). The invasive mapping system enables potential measurements together with information about the recording site. The invasively measured endocardial AT map of the right ventricle was compared to the calculated endocardial activation times, obtained from 62–channel BSPM data. The results were in good qualitative agreement, and the correlation coefficient for the measured and calculated activation times was found to be 0.84.

In Publications VII and VIII, the UDL model has been used in calculating activation times in four patients from 67–channel MCG and 123–channel BSPM recordings. In the validation of the results, invasively measured epicardial electrograms were used to construct the reference epicardial activation times. The invasive data were recorded during arrhythmia surgery from the epicardial surfaces of the patients with a 102–channel socket electrode system (CardioLab$^{\mathrm{R}}$ Prucka Engineering, Inc., Houston, TX, USA). Based on MR images, an individual BE torso model was constructed for each patient, including the torso boundary,

the lungs, and the cavities within the heart. The ventricular surface, including both epi– and endocardium, was also reconstructed from the MR images. An algorithm was developed which allowed the mapping of the invasive data on the epicardial surface of the heart. The algorithm simulated the positioning of the electrode sock around the heart on basis of a sketch made during surgery. In Publication VII, the activation times computed from the BSPM recordings were compared to the invasive data. Publication VIII presents a comparison between the activation times produced from MCG and BSPM data, and the invasive data. The overall patterns of activation in the reference data were reproduced relatively well in the activation time maps computed from MCG and BSPM data. However, precise locations for the early and late activation spots could not be found from the calculated activation time maps. All patients included in Publications VII and VIII had previously suffered from myocardial infarctions. The UDL model is based on the assumption of a uniform source strength surrounding the whole ventricular muscle. This assumption is not valid for infarcted regions, which, no doubt, cause some of the differences found between the measured and computed activation times. In addition, the uncertainty of approximately 1–2 cm in the epicardial electrode locations likely affects the comparison between the measured and the calculated activation times.

In Fig. 11, an example of the measured and the calculated activation times on the epicardial surface of the heart is presented. The isocontours of the activation times are shown with a step of 5 ms. The measured activation times have been interpolated between the epicardial electrode locations. The activation time map generated from the measured data shows an early spot on the anterior surface of the RV. Another site of early activation is found in the latero–basal region of the LV. Late activation is detected in the apical region. In the activation time map calculated from BSPM data, early activation is detected on the anterior surface of the RV, and also in the apical region. Late activation is found between the two sites of early activation, and in the basal regions of the LV. In the activation times computed from MCG data, early activation is located on the anterior surface of the RV, as well as in the lateral and postero–basal regions of the LV. Late activation is detected in the apical region. Therefore, in the MCG based UDL solution, the overall pattern of activation is reproduced relatively well while in the BSPM solution, the activation pattern on the anterior surface of the RV is somewhat shifted with respect to the measured data.

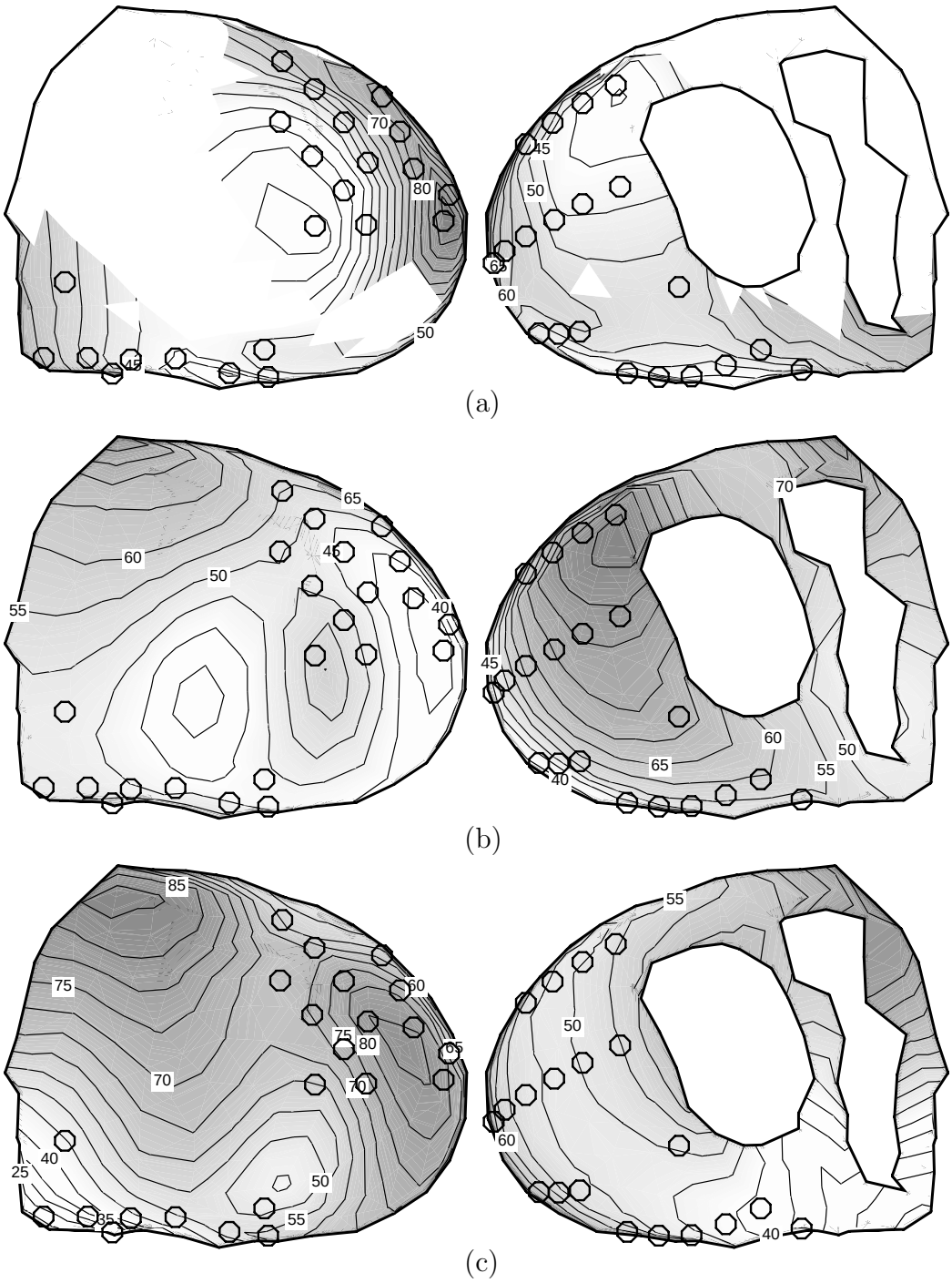

Fig. 11: *An example of the comparison between a) the measured, b) the calculated BSPM and c) the calculated MCG activation times, presented on an anterior and on a posterior projection of the ventricular epicardial surface. The lightest and darkest gray indicate earliest and latest activation, respectively. The activation times are shown in milliseconds. The locations of the epicardial electrodes are marked with circles.*

6 Cardiomagnetic instrumentation

In the following, the multichannel instrumentation used in cardiomagnetic studies is briefly described. The main focus is on the BioMag Laboratory, where all the magnetic measurements used in this thesis were performed. A comprehensive list of multichannel SQUID devices currently employed in biomagnetic studies (brain and heart) has recently been presented by Nowak (1998).

6.1 BioMag Laboratory

The BioMag Laboratory at HUCH, founded in 1995, has state–of–the–art facilities both for basic research and for clinical applications in functional bioelectromagnetic cardiac and brain studies. In a three–layer high–performance magnetically shielded room, providing shielding against ambient urban magnetic noise (Paavola *et al* 2000), a 122–channel neuromagnetometer (Knuutila *et al* 1993) and a 67–channel cardiomagnetometer have been installed. An outer view of the shielded room is presented in Fig. 12a. In addition, a 64–channel bioelectric recording system designed for simultaneous use with biomagnetic recordings (Virtanen *et al* 1997), a 128–channel portable BSPM system (Simelius 1998), modern imaging facilities in HUCH, including anatomical and functional MRI, and a fast asynchronous transfer mode (ATM) network in the hospital and between the Finnish universities, give a unique framework for the studies.

The 67–channel cardiomagnetometer was designed and constructed in collaboration between Neuromag Ltd., Helsinki, and the Laboratory of Biomedical Engineering at Helsinki University of Technology (Montonen *et al* 2000). The cardiomagnetometer is presented in Fig. 12b. The sensor array consist of seven axial and 60 planar DC (direct current) SQUID gradiometers in a hexagonal grid. The channel layout is presented in Fig. 13. The functioning of SQUID detectors will not be handled here; it has been described in detail, e.g., by Katila (1989). The wire–wound axial first–order gradiometers have a baseline of 80 mm; the pick–up coil radius is 37.5 mm. The thin–film planar gradiometers have a baseline of 16.2 mm, and they are arranged in 30 units which consist of two perpendicular figure–of–eight loops. The magnetic field component perpendicular to the surface of a sensor is described by B_z. The axial gradiometers measure the change in B_z along the surface normal of the sensor ($\partial B_z/\partial z$), while the planar gradiometers measure the change in B_z parallel to the sensor surface ($\partial B_z/\partial x$ and $\partial B_z/\partial y$). Four planar units, located at the edge of the array, are positioned perpendicularly to the dewar bottom, while the other 26 units are parallel to the bottom. The system is modular in the sense that the axial and planar gradiometers are interchangeable. High sensitivity of the gradiometers was reached by minimizing the magnetic noise caused by the conducting materials inside the measurement dewar (Nenonen *et al* 1996); the noise levels are about 3 fT/$\sqrt{\text{Hz}}$ for axial and 3 fT/cm$\sqrt{\text{Hz}}$ for planar sensors

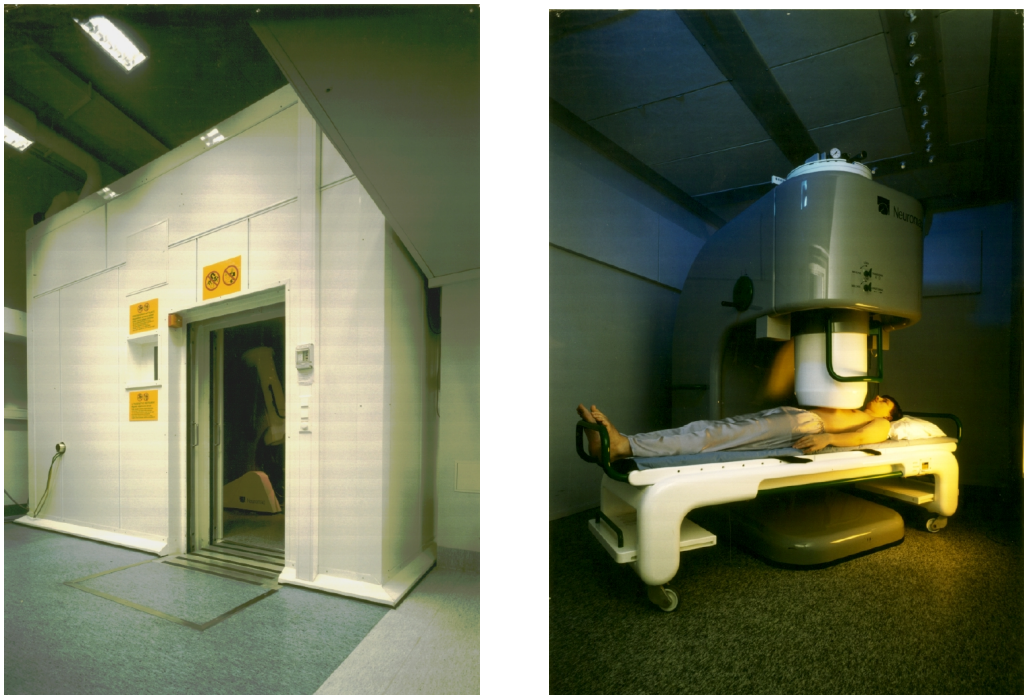

(a) (b)

Fig. 12: *a) The magnetically shielded room and b) the 67–channel cardiomagnetometer of the BioMag Laboratory, located at the Helsinki University Central Hospital.*

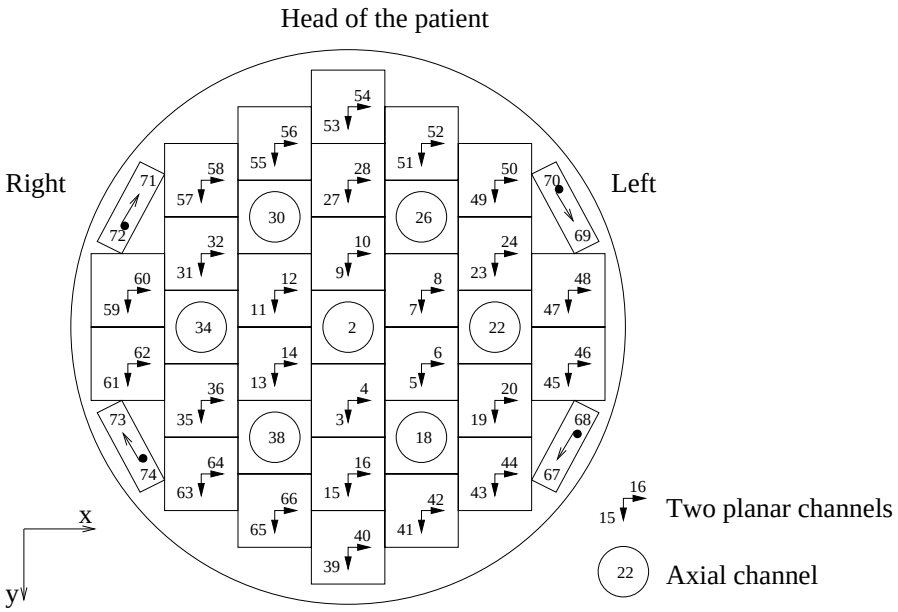

Fig. 13: *The 67–channel layout of the cardiomagnetometer at the Biomag Laboratory. The numbering of the channels starts from two. Two numbers are used also in the axial units even though they contain only one channel.*

(frequency range from 5 Hz to 100 Hz).

The sensors are immersed in liquid helium inside a 130 cm long cylindrical dewar with inner and outer diameters of 30 cm and 42 cm, respectively. The dewar has a cylindrically curved bottom with a radius of curvature of 80 cm. The distance from the liquid helium space to the outer surface of the dewar is 2.5 cm. The dewar is supported by a gantry which can be moved on an air cushion. The gantry system allows both vertical adjustment and tilting by 20 degrees in any direction. During recording the patient is lying on a wheeled non–magnetic bed.

The measurement protocol in the cardiomagnetic recordings varies among different patient groups. A typical measurement can be described as follows: In the preparation phase, the ECG leads and three magnetic–field generating coils, used in indicating the patient's position with respect to the dewar, are attached on the chest. The coordinates of the coils and other landmarks on the chest are stored using a three–dimensional digitizer (3SPACE$^{\mathrm{R}}$, Polhemus Inc., Colchester, VT, USA). After the preparations, the patient is taken into the magnetically shielded room on the wheeled bed and the dewar is positioned over the chest. In the beginning of the recording session, the position of the sensor array with respect to the patient is measured utilizing the above mentioned three coils. Typically, data are collected for 2–5 minutes with a Hewlett–Packard (Palo Alto, CA, USA) data acquisition unit connected to a real–time processor, controlled by an HP9000 workstation. The anti–aliasing filter and the sampling rate are software–adjustable. Normally, the data are band–pass filtered to 0.03–300 Hz and digitized with a sampling rate of 1000 Hz.

6.2 Other research sites

The Physikalisch–Technische Bundesanstalt (PTB) in Berlin, Germany, has designed and built a non–commercial sensitive multichannel measurement device with 83 SQUIDs (Drung 1995). The system consists of seven 11–SQUID modules plus six single–channel modules. A total of 63 magnetometers are oriented to detect B_z, the remaining 20 sensors are detecting B_x and B_y. The magnetometers are located at four levels which are parallel to the flat dewar bottom. This system allows the realization of first– or second–order gradiometers, depending on the measurement requirements. The distance between the sensor level and outer dewar bottom is approximately 25 mm. The diameter of the area covered with magnetometers in the sensor level is about 21 cm.

Friedrich Schiller University of Jena, Germany, has a twin–dewar biomagnetometer system with 2 $\times$ 31 channels, designed and manufactured by Philips (Hamburg, Germany). The symmetrical first–order axial gradiometers have a diameter of 2 cm and a baselength of 7 cm (Dössel *et al* 1993). In addition to the single–dewar recordings, MCG can be measured in two planes over the chest with the double–dewar construction. Additionally, 62 ECG

channels can be recorded simultaneously with the MCG.

A 74–channel two–dewar system of Biomagnetic Technologies Inc. (BTi, San Diego, CA), presently 4–D NeuroImaging, has been installed at the Friedrich Alexander University of Erlangen, Germany. The system contains two 37–channel dewars which allow simultaneous measurements from the anterior and posterior side of the chest. The detectors are first–order axial gradiometers with diameters of 2.2 cm and 2.4 cm, and a baseline of 5 cm. The sensors are covering an area of 14.4 cm in diameter.

At FEMT Bochum, a 70–channel system of BTi was installed in 1997. This system has been designed primarily for cardiac studies with a concave measuring surface and an outer radius of 52 cm. It utilizes 67 magnetometers with a diameter of 2.8 cm in a circular arrangement with a diameter of 32 cm. 61 magnetometers are oriented approximately parallel to the sensor axis while six coils are measuring the transversal field component.

A 55–channel MCG system by Advanced Technologies Biomagnetics (AtB) has been installed at the University of Ulm and Chieti in 1998 (Erné *et al* 1999). This device consists of 77 magnetometers with a diameter of approximately 0.8 cm. The lowest (sensor) level contains 55 magnetometers, and 7 cm above the sensor level there are 19 magnetometers acting as compensation coils. The third (highest) level, 14 cm above the sensor level, has a triplet of magnetometers oriented in the x–, y– and z–directions. The magnetometers in the sensor level are located in a hexagonal grid with a grid constant of 3.2 cm. First– and second–order gradiometers can be applied by software.

In Japan, there are also groups working on the MCG, e.g., at Tokyo Denki University, there is a 39–channel device with 3D second–order gradiometers (Kobayashi and Uchikawa 1999). The system is suitable for brain and heart studies.

6.3 Requirements and future development

In order for the instrumentation to be applicable for cardiomagnetic source imaging studies, a high enough SNR will have to be achieved in the measurements. Often this leads to performing the recordings in a magnetically shielded room. This prevents, for example, the measurements in a catheterization laboratory, and even excludes some patients from the MCG studies. With higher–order gradiometers and active noise compensation, however, it is possible to perform measurements outside of a magnetically shielded room and still obtain a reasonable SNR for data analysis. In addition, the sensors should cover a wide enough area over the chest to capture the variations in the field patterns in order to obtain reliable source imaging results.

With an increasing number of MCG patients measured at different research sites, more attention has been given to the compatibility and comparability of the data. Burghoff *et al* (2000) studied two transformation procedures, a multipole expansion and minimum norm

estimation, to compare MCGs recorded at PBT and at BioMag. They found that the methods were useful in transforming MCG recordings into another sensor configuration.

One of the future trends in cardiomagnetic instrumentation most likely includes the development of the multichannel cardiomagnetometers into devices which could be operated in a fully clinical environment. As an example of such a development, a multichannel cardiomagnetometer with second–order gradiometers will be installed at the Catholic University of Rome in a catheterization laboratory in the near future. Special attention will be paid to minimize the size of the bottom of the dewar in order not to disturb the clinical interventions. The technique of resolving the position of the tip of a stimulation catheter, investigated also in this thesis, will be taken into standard clinical use. The MCG measurements and subsequent localizations can be expected to reduce the time required for the treatment of the patient. The results obtained with this system can be used in developing multichannel MCG devices more suitable for a clinical environment.

The progress in the development of high–temperature (HT_C) SQUIDs, which can be operated even at 70–80 K and therefore be cooled with liquid nitrogen, is likely to produce compact recording units that could be operated at a patient's bedside or in a very lightly magnetically shielded room. The operational difficulties and costs of such a device would be substantially smaller than those of the current LT_C devices. However, the sensitivity of the HT_C SQUIDs is still somewhat lower than in LT_C SQUIDs. Test measurements carried out with a HT_C sensor in the Berlin magnetically shielded room showed a sensitivity of 49 $fT/\sqrt{Hz}$ from 40 Hz onward and an RMS value of 0.9 pT for the noise (Lindström 1999).

7 Discussion

In this thesis, different source and volume conductor models, applicable for cardiomagnetic source imaging studies, were investigated. In some cases, also body surface potential mapping recordings were used for comparison purposes. The localization results were validated invasively, e.g., by using a non–magnetic catheter inserted in the heart, and by epicardial potential recordings carried out during an open–chest surgery. The calculations were performed with boundary element models, including piecewise homogeneous electric conductivity inside the thorax. In the following, some aspects related to the calculations, such as the effect of anisotropic parts inside the thorax, are considered. In addition, the role of magnetic measurements is evaluated versus electric recordings and other imaging techniques suitable for obtaining functional information about the heart. Finally, possible future trends in cardiomagnetic source imaging techniques are addressed.

7.1 The role of anisotropy

In the studies performed in this thesis, the boundary element method (BEM) was used in describing the properties of the volume conductor, assuming a piecewise homogeneous electric conductivity. If anisotropies of the electric conductivity would be included in the calculations, the finite element method (FEM) would be required. In FEM, a full domain mesh of the volume conductor, consisting of volume elements, is required. The dimensions of the system matrices in FEM are considerably larger than in BEM. However, efficient sparse matrix techniques can be used to speed up the calculations.

Several studies have been carried out concerning the effect of the anisotropy of the heart. For example, Wei *et al* (1995) simulated an isotropic and anisotropic heart where the anisotropy of conduction velocity and intracellular electric conductivity were included. Simulations of the normal heart, and left and right bundle branch blocks showed no significant differences between the two models in the excitation processes of the whole heart or in the body surface electrocardiograms. Thivierge *et al* (1997) used the ECD in defining the effect of fiber direction in a layered inner block representing the heart. Current dipoles of different orientations were placed in the inner block and the potentials calculated everywhere. Effects of the anisotropy of the inner block were gauged by computing ECD localizations from the outer block surface potentials. For volume conductor conductivities close to that of the torso, the anisotropy was found to diminish dipoles oriented along the fibers.

In addition to the heart, other parts of the body may also show a certain degree of anisotropy. The effect of the anisotropic skeletal muscle layer has been investigated, e.g., by Gulrajani and Mailloux (1983), and it has been found to have a prominent effect on body surface potentials (Klepfer *et al* 1997). The effect of the skeletal muscle on ECD localizations was simulated by Bruder *et al* (1994b) who found that including the skeletal muscle layer

in an approximative manner smoothed the surface potential which in turn produced too deep BSPM dipole localizations. However, the corresponding magnetic field pattern was less affected by the skeletal muscle layer. This could also account for the differences in MCG and BSPM localization results in Publication III.

Despite the results of some studies pointing out differences in the generated fields calculated with isotropic and anisotropic volume conductor models, the practical requirements in clinical work, demanding nearly on–line localization results, often make it impossible to assign individual fiber directions in the heart and, e.g., in the skeletal muscle layer. However, in the future it would be beneficial to develop methods which would enable an easy inclusion of the appropriate anisotropies in the cardiomagnetic source imaging studies.

7.2 MCG vs. ECG

The superiority of MCG over ECG, or vice versa, has been the subject of an ongoing discussion. It has even been suggested that MCG can be derived from ECG measurements (van Oosterom *et al* 1990), and therefore the magnetic measurements would be unnecessary. In the following, some theoretical points of view and experimentally observed phenomena will be discussed.

7.2.1 Theoretical considerations

It is evident that ECG and MCG are sensitive to different configurations of the source current: body surface potential measurements reflect the flux of the primary current distribution whereas the magnetic measurements are associated with the curl of the same source (e.g., Plonsey 1972). Therefore, certain source configurations can be undetectable in one measurement but visible in the other. For example, a radial dipole in a semi–infinite halfspace or in a sphere produces no magnetic signal outside the volume conductor. In a more complex volume conductor, however, a radial dipole produces a magnetic signal due to the secondary currents on the boundaries. On the other hand, a vortex type of current, i.e. a current loop, would be undetectable in ECG measurements, but generates a measurable magnetic field.

Differences between the observed electric and magnetic signals have also been investigated by using the bidomain model of the heart. Studies about “electrically silent” magnetic fields have been presented, e.g., by Roth and Wikswo (1986) and by Fischer *et al* (1999b). Such magnetic fields arise from a helix or spiral like fiber architecture where off–diagonal terms enter into the conductivity tensors of the bidomain model. Roth and Wikswo (1986) suggested that the apex of the heart is an obvious example of a tissue with a spiraling cellular geometry.

7.2.2 Experimental observations

In physical and pharmacological exercise studies (Brockmeier *et al* 1994, 1997), more distinct changes in multichannel MCG signals than in the simultaneously recorded 32–lead ECG maps have been reported. A vortex source, which would be undetectable in ECG measurements, was suggested to explain the phenomenon.

Considering clinical use, the fetal MCG recordings are an important application of magnetic measurements. They have shown to detect the heart rate of the fetus and even some cardiac abnormalities throughout the course of pregnancy (e.g., Kariniemi *et al* 1974, Hukkinen *et al* 1976, Quinn *et al* 1994, Wakai *et al* 1997, Hamada *et al* 1999, van Leeuwen *et al* 1999). The magnetic recordings are specially important because the ECG signal of a fetus decreases after the 25th week of gestation and becomes practically undetectable while the MCG signal increases. After the 30th week, the ECG signal increases again together with the MCG signal. The decrease of the electric signal is caused by vernix caseosa, an insulating layer covering the fetus (e.g., Oostendorp and van Oosterom 1991).

In addition to fetal recordings, Moshage *et al* (1991) found that MCG was superior to ECG in the quantification of the left ventricular hypertrophy (LVH). Recently Takala *et al* (2000) reported a study of 13 hypertensive patients in whom the degree of hypertrophy was measured using echocardiographic studies. The performance of the MCG was compared to the standard 12–lead ECG. The analysis method used in the MCG was the measure of the QRS area scaled to the distance of the heart from the measurement dewar. The MCG results showed a good correlation of 0.70 ($p = 0.007$) with the echocardiographic results while the ECG results did not correlate significantly with the echocardiography (0.56, $p = 0.27$). According to this preliminary small–scale study, MCG could provide a practical screening method for the detection of pathologic LV hypertrophy in hypertensive patients.

On the other hand, the applicability of multichannel BSPM mapping for an on–line use in a catheterization laboratory is an advantage of the electric recordings over the magnetic ones. The BSPM pace–mapping studies (e.g., Liebman *et al* 1991, Dubuc *et al* 1993, SippensGroenewegen *et al* 1993, Simelius *et al* 1996) have shown to successfully guide catheter ablations during the procedure. The MCG localizations will usually have to be performed in a separate session. In addition, anatomical information about the patient is required to produce an individual description of the torso.

Therefore, the question whether the information in MCG mapping is superior to BSPM, or vice versa, still does not have a clear answer. Nevertheless, it is evident that both mapping methods, employed either separately or in combination, can provide diagnostic information which is superior to the standard 12–lead ECG. Especially, combining electric and magnetic recordings could produce additional information in the clinical evaluation of the patients. For example, it has been suggested that isocontour maps derived from multichannel MCG

and BSPM data provide complementary means of discriminating between normal subjects and myocardial infarction patients (Lant *et al* 1990). However, the costs associated with a multichannel MCG system are substantial compared to that of an ECG measuring system. Therefore, until nowadays MCG systems have mainly been used as research tools.

7.3 Other functional imaging techniques

Bioelectric and –magnetic studies offer functional information about electrically active organs, such as the heart and the brain, which is difficult to obtain by other imaging techniques. For example, MRI, computed tomography (CT) and X–ray imaging mainly provide only anatomical information. The alternative functional imaging methods, such as perfusion–MRI, PET and single photon emission computed tomography (SPECT), involve the use of intravenous markers to produce knowledge about metabolic processes. In addition, the time resolution of perfusion–MRI, PET and SPECT is only around one second while with MCG/ECG, information is obtained within millisecond time resolution.

In addition to measurements carried on and outside of the body, electric and magnetic recordings have also been performed inside the heart. For example, an intracavitary multielectrode probe has been applied in recording cardiac activity. It has been stated that due to smoothing, the potential distribution measured on the probe does not accurately enough reflect the local changes in the cardiac activity, and therefore an inverse procedure is needed to reconstruct the endocardial potential distribution (Khoury and Rudy 1992). Khoury *et al* (1995) found an accuracy of 10–20 mm in reconstructing local events of cardiac excitation, e.g. pacing sites, by solving the endocardial potential distribution from the multielectrode probe recordings in the cavity of an isolated canine left ventricle. To be applicable in a catheterization laboratory, however, the method requires the determination of the probe–cavity geometry. Recently, Liu *et al* (1998) suggested using a small multielectrode catheter that could be introduced percutaneously, and found that a catheter with a curved geometry performed well in reconstructing the endocardial potentials.

7.4 Future aspects

Magnetocardiographic recordings have many advantages to become a clinical method. First of all, they are fully non–invasive. Current multichannel MCG systems are also very fast; a patient measurement can be carried out in a few minutes. Therefore, the safety and the comfort of the patient are high. One MCG measurement can offer several electromagnetic parameters for a thorough characterization of the patient's heart. The high quality of the inverse solutions obtained in the studies carried out in this thesis prompts the use of cardiomagnetic source imaging in several clinical applications.

The high accuracy of ECD localizations, observed in this thesis, encourages the on–line

use of the method during EP studies. The necessary developments in the instrumentation were previously described. However, in order to obtain high–quality localizations, individual torso models are required in the inverse calculations. The cost and the availability of MRI might reduce the clinical use of the method. Obtaining the torso models, e.g., from X–ray images, where the positions of the lungs and the heart can be approximated, would reduce the costs and improve the availability of source imaging results. The construction of such models has been investigated by Lötjönen *et al* (1999b) who found that the average error in the positions of the nodes in the BE model, produced by the X–ray modeling, was about 5 mm. Such an accuracy of the torso model is adequate for most source imaging purposes. Therefore, the ECD localization method could be developed into a clinical tool to be used in a catheterization laboratory.

The preliminary studies about localizing ischemia from MCG recordings show the promise of the technique. Detection and localization of ischemia and viability would concern a large number of cardiac patients, if the MCG method proves to be useful. The results obtained in this thesis show the potential of the MCG method to identify ischemic regions on the surface of the left ventricle. While in this thesis the effect of the geometry and topology of the BE model was thoroughly investigated as a function of the ECD localization accuracy, further studies are needed to investigate the effect of the volume conductor model on the current density estimation result.

The calculation of activation times on the epi– and endocardial surfaces of the ventricular muscle was also found to be a promising method for imaging the ventricular function. By using the UDL as the source model, the whole depolarization phase can be represented with a single inverse solution. The quality of the activation times calculated in this thesis was most likely reduced by the large infarcted areas of the patients for which the assumption about a uniform source strength does not hold. Therefore, further validation studies with structurally healthy hearts and exact references about the ventricular function would be required to optimally discover the potential of this inverse solution. Ideally, the same reference data could be used in studying the properties of all source models investigated in this thesis.

Acknowledgments

The thesis was made at the Laboratory of Biomedical Engineering at the Helsinki University of Technology. All magnetocardiographic and body surface potential recordings were carried out at the Helsinki University Central Hospital. A large part of the work was done in co–operation with professor Riccardo Fenici from the Catholic University of Rome, Italy. Other foreign collaborators were Dr. Thom Oostendorp from the University of Nijmegen, the Netherlands, and Dr. Uwe Tenner from the University of Ilmenau, Germany.

I would like to thank my supervisor, professor Toivo Katila, for creating excellent conditions for the research work and for his support. My director, Dr. Jukka Nenonen, deserves my gratitude for the inspiring research ideas and for his collaboration. I am extremely grateful to professor Riccardo Fenici for having the opportunity to work with him. The results of the co–operation form a significant part of this thesis. A warm thank you is given to other foreign collaborators, as well. To Dr. Risto Ilmoniemi I am grateful for the excellent measurement facilities at the BioMag Laboratory. To Dr. Jyrki Lötjönen I want to express my thanks for the preparation of the numerous boundary element models, and for the collaboration and enjoyable discussions we have had. Mr. Panu Takala deserves my warmest thanks for the non–magnetic exercise ergometer. I am also grateful to Mr. Kim Simelius for his support in the body surface potential mapping recordings. All the other colleagues at the Laboratory of Biomedical Engineering deserve my thanks for the nice and stimulating atmosphere at the laboratory.

I am also indebted to the medical collaborators from HUCH. I wish to express my warmest thanks to Dr. Lauri Toivonen and Dr. Markku Mäkijärvi for their collaboration and research ideas, as well as to Ms. Helena Hänninen and Mr. Petri Korhonen for their clinical contribution to the thesis. Them and others involved, especially Ms. Leila Sikanen, I would like to thank for performing numerous MCG and BSPM measurements.

To my husband Marko I am grateful for the eternal flame which he has brought into my life, as well as for the continuous encouragement he has offered me during the preparation of the thesis. My parents Leila and Heikki deserve my gratitude for the support and trust they have always given me. To all my friends, especially Heli, Antti, Elisa and Esa, I am thankful for all the joyful encounters and celebrations we have had which have efficiently captured my thoughts from research work into quite something else.

The financial support of the Academy of Finland, Helsinki University of Technology, the Progress of Technology Foundation, Finnish Cultural Foundation, Eemil Aaltonen Foundation, and Jenny and Antti Wihuri Foundation is gratefully acknowledged.

Espoo, April 10, 2000

Katja Pesola

References

Ahmad G, Brooks D and MacLeod R 1998: An admissible solution approach to inverse electrocardiography *Ann. Biomed. Eng.* **26** 278–292

Barnard A, Duck I and Lynn M 1967a: The application of electromagnetic theory to electrocardiology I: Derivation on the integral equations *Biophys. J.* **7** 443–462

Barnard A, Duck I, Lynn M and Timlake W 1967b: The application of electromagnetic theory to electrocardiology II: Numerical solution of the integral equations *Biophys. J.* **7** 463–491

Barr R C, Ramsey M and Spach M S 1977: Relating epicardial to body surface potential distributions by means of transfer coefficients based on geometry measurements *IEEE Trans. Biomed. Eng.* **24** 1–11

Baule G and McFee R 1963: Detection of the magnetic field of the heart *Am. Heart J.* **55** 95–98

Baule G and McFee R 1970: The magnetic heart vector *Am. Heart J.* **79** 223–236

Brebbia C A, Telles J C and Wrobel L C 1984: *Boundary Element Techniques – Theory and Applications in Engineering* (Berlin: Springer–Verlag)

Brockmeier K, Comani S, Erné S N, Di Luzio S, Pasquarelli A and Romani G L 1994: Magnetocardiography and exercise testing *J. Electrocardiol.* **27** 137–142

Brockmeier K, Schmitz L, Chavez J, Burghoff M, Koch H, Zimmermann R and Trahms L 1997: Magnetocardiography and 32–lead potential mapping: the repolarization in normal subjects during pharmacologically induced stress *J. Cardiovasc. Electrophysiol.* **8** 615–626

Brooks D H, Ahmad G F, MacLeod R S and Maratos G M 1999: Inverse electrocardiography by simultaneous imposition of multiple constraints *IEEE Trans. Biomed. Eng.* **46** 3–18

Bruder H, Killmann R, Moshage W, Weismüller P, Achenbach S and Bömmel F 1994a: Biomagnetic localization of electrical current sources in the human heart with realistic volume conductors using the single–current–dipole model *Phys. Med. Biol.* **39** 655–668

Bruder H, Scholz B and Abraham–Fuchs K 1994b: The influence of inhomogeneous volume conductor models on the ECG and the MCG *Phys. Med. Biol.* **39** 1949–1968

Burghoff M, Nenonen J, Trahms L and Katila T 2000: Conversion of magnetocardiographic recordings between two different multichannel SQUID devices *IEEE Trans. Biomed. Eng.* in press

Clements J, Carroll R and Horáček B M 1994: On regularization parameters for inverse problems in electrocardiography *Biomedical Physics Horizons* Ed. D Ghista (Wiesbaden: Vieweg Verlag) 235–246

Cohen D, Norman J C, Molokhia F and Hood W Jr 1971: Magnetocardiography of direct currents: S–T segment and baseline shifts during experimental myocardial infarction *Science* **172** 1329–1333

Cohen D and Hosaka H 1976: Magnetic field produced by a current dipole *J. Electrocardiol.* **9** 409–417

Cohen D, Savard P, Rifkin R D, Lepeschkin E and Strauss W E 1983: Magnetic measurement of S–T and T–Q segment shifts in humans. Part II: Exercise–induced S–T segment depression *Circ. Res.* **53** 274–279

Cuffin B N and Geselowitz D 1977: Studies of the electrocardiogram using realistic cardiac and torso models *IEEE Trans. Biomed. Eng.* **24** 242–252

Czapski P, Ramon C, Huntsman L L, Bardy G H and Kim Y 1996: On the contribution of volume currents to the total magnetic field resulting from the heart excitation process: A simulation study *IEEE Trans. Biomed. Eng.* **43** 95–104

Czapski P, Ramon C, Haueisen J, Huntsman L L, Nowak H, Bardy G H, Leder U and Kim Y 1998: MCG simulations of myocardial infarctions with a realistic heart–torso model *IEEE Trans. Biomed. Eng.* **45** 1313–1322

Drung D 1995: The PTB 83–SQUID system for biomagnetic application in a clinic *IEEE Trans. Appl. Supercond.* **5** 2112–2117

Dubuc M, Nadeau R, Tremblay G, Kus T, Molin F and Savard P 1993: Pace mapping using body surface potential maps to guide catheter ablation of accessory pathways in patients with Wolff–Parkinson–White syndrome *Circulation* **87** 135–143

Durrer D, van Dam R, Freud G, Janse M, Meijler F and Arzbaecher R 1970: Total excitation of the isolated human heart *Circulation* **41** 899–912

Dössel O, David B, Fuchs M, Krüger J, Lüdeke K M and Wischmann H A 1993: A 31–channel SQUID system for biomagnetic imaging *Appl. Superconductivity* **1**(10–12) 1813–1825

Erné S N, Pasquarelli A, Kammrath H, Della Penna S, Torquati K, Pizzella V, Rossi R, Granata C and Russo M K 1999: Argos 55 – The new MCG system in Ulm *Recent Advances in Biomagnetism: Proceedings of the 11th International Conference on Biomagnetism* Eds. T Yoshimoto *et al* (Sendai: Tohoku University Press) 27–30

Fenici R and Melillo G 1993: Magnetocardiography: ventricular arrhythmias *Eur. Heart J.* **14** (Suppl. E) 53–60

Fenici R, Fenici P and van Bosheide J 1996: Amagnetic catheter for biomagnetically guided endocardial mapping and ablation of cardiac arrhythmias *Micro System Technologies* Eds. H Reichl and A Heuberger (Berlin: VDE–Verlag GmbH) 711–716

Fenici R, Pesola K, Mäkijärvi M, Nenonen J, Tenner U, Fenici P and Katila T 1998: Nonfluoroscopic localization of an amagnetic catheter in a realistic torso phantom by magnetocardiographic and body surface potential mapping *Pacing Clin. Electrophysiol.* **21** 2485–91

Ferguson A S, Zhang X and Stroink G 1994: A complete linear discretization for calculating the magnetic field using the boundary element method *IEEE Trans. Biomed. Eng.* **41** 455–460

Ferguson A S and Stroink G 1995a: Localization of epicardial sources using magnetic and potential maps *Biomagnetism: Fundamental Research and Clinical Applications* Eds. C Baumgartner *et al* (Amsterdam: Elsevier Science/IOS Press) 641–646

Ferguson A S, Vardy D, Hren R and Stroink G 1995b: A regularized minimum norm method for calculating distributions of source currents on epicardial surfaces *Biomagnetism: Fundamental Research and Clinical Applications* Eds. C Baumgartner *et al* (Amsterdam: Elsevier Science/IOS Press) 676–679

Ferguson A S and Stroink G 1997: Factors affecting the accuracy of the boundary element method in the forward problem – I: Calculating surface potentials *IEEE Trans. Biomed. Eng.* **44** 1139–1155

Fischer G, Tilg B, Wach P, Lafer G and Rucker W 1998: Analytical validation of the BEM – application of the BEM to the electrocardiographic forward and inverse problem *Comput. Methods Programs Biomed.* **55** 99–106

Fischer G, Tilg B, Wach P, Modre R, Leder U and Nowak H 1999a: Application of high–order boundary elements to the electrocardiographic inverse problem *Comput. Methods Programs Biomed.* **58** 119–131

Fischer G, Tilg B, Modre R, Fetzer J, Rucker W, Huiskamp G and Wach P 1999b: The electrically silent cardiac magnetic field *Biomed. Techn.* **42** (Suppl. 1) 273–276

Forsman K, Nenonen J, Purcell C J and Stroink G 1992: Biomagnetic inverse solution with a realistic torso model *Advances in Biomagnetism '91: Clinical Aspects* Eds. M Hoke *et al* (Amsterdam: Elsevier) 819–823

Frijns J, de Snoo S and Schoonhoven R 2000: Improving the accuracy of the boundary element method by the use of second order interpolation functions *IEEE Trans. Biomed. Eng.* in press

Geddes L A and Baker L E 1967: The specific resistance of biological material – a compendium of data for the biomedical engineer and physiologist *Med. Biol. Eng.* **5** 271–293

Gençer N and Tanzer I 1999: Forward problem solution of electromagnetic source imaging using a new BEM formulation with higher–order elements *Phys. Med. Biol.* **44** 2275–2287

Geselowitz D 1967: On bioelectric potentials in an inhomogeneous volume conductor *Biophys. J.* **7** 1–11

Geselowitz D 1970: On the magnetic field generated outside an inhomogeneous volume conductor by internal current sources *IEEE Trans. Magn.* **6** 346–347

Geselowitz D and Miller W T 1983: A bidomain model for anisotropic cardiac muscle *Ann. Biomed. Eng.* **11** 191–206

Golub G, Heath M and Wahba G 1979: Generalized cross–validation as a method for choosing a good ridge parameter *Technometrics* **21** 215–223

Gorodnitsky I, George J and Rao B 1995: Neuromagnetic source imaging with FOCUSS: a recursive weighted minimum norm algorithm *EEG and Clinical Neurophysiology* **95** 231–251

Greensite F 1995: Remote reconstruction of confined wavefront propagation *Inverse Problems* **11** 361–370

Gulrajani R M and Mailloux G E 1983: A simulation study of the effects of torso inhomogeneities on electrocardiographic potentials, using realistic heart and torso models *Circ. Res.* **52** 45–56

Gulrajani R M, Pham–Huy H, Nadeau R, Savard P, De Guise J, Primeau R and Roberge F A 1984: Application of the single moving dipole inverse solution to the study of the Wolff–Parkinson–White syndrome in man *J. Electrocardiol.* **17** 271–288

Hamada H, Horigome H, Asaka M, Shigemitsu S, Mitsui T, Kubo T, Kandori A and Tsukada K 1999: Prenatal diagnosis of long QT syndrome using fetal magnetocardiography *Prenat. Diagn.* **19** 677–680

Hansen P 1992: Analysis of discrete ill–posed problems by means of the L–curve *SIAM Rev.* **34** 561–580

Hansen P and O'Leary D 1993: The use of the L–curve in the regularization of discrete ill–posed problems *SIAM J. Sci. Comput.* **14** 1487–1503

Horáček B M 1973: Digital model for studies in magnetocardiography *IEEE Trans. Magn.* **9** 440–444

Horáček B M, Purcell C J, Lamothe R, Merritt R, Kafer C, Periyalwar S, Dey S, Leon L J and Stroink G 1987: The effect of torso geometry on magnetocardiographic isofield maps *Phys. Med. Biol.* **32** 121–124

Horáček B M and Clements J 1997: The inverse problem of electrocardiography: A solution in terms of single– and double–layer sources on the epicardial surface *Math. Biosci.* **144** 119–154

Hren R, Zhang X and Stroink G 1996: Comparison between electrocardiographic and magnetocardiographic inverse solutions using the boundary element method *Med. Biol. Eng. Comput.* **34** 110–114

Hren R, Stroink G and Horáček B M 1998: Accuracy of single–dipole inverse solution when localising ventricular pre–excitation sites: simulation study *Med. Biol. Eng. Comput.* **36** 323–329

Hubley–Kozey C L, Mitchell B, Gardner M J, Warren J W, Penney C J, Smith E R and Horáček B M 1995: Spatial features in body–surface potential maps can identify patients with a history of sustained ventricular tachycardia *Circulation* **92** 1825–38

Huiskamp G and van Oosterom A 1988: The depolarization sequence of the human heart surface computed from measured body surface potentials *IEEE Trans. Biomed. Eng.* **35** 1047–1058

Huiskamp G 1991: Difference formulas for the surface Laplacian on a triangulated surface *J. Comp. Phys.* **95** 477–496

Huiskamp G, Oostendorp T, Pijls N and van Oosterom A 1992: Invasive confirmation of the human ventricular activation sequence as computed from body surface potentials *Computers in Cardiology* Ed. R Werner (Los Alamitos: IEEE Computer Society Press) 427–430

Huiskamp G and Greensite F 1997: A new method for myocardial activation imaging *IEEE Trans. Biomed. Eng.* **44** 433–446

Hukkinen K, Kariniemi V, Katila T, Laine H, Lukander R and Mäkipää P 1976: Instantaneous fetal heart rate monitoring by electromagnetic methods *Am. J. Obstet. Gynecol.* **125** 1115–1120

Hämäläinen M and Ilmoniemi R 1984: Interpreting measured magnetic fields of the brain: estimates of current distributions *Report TKK–F–A559* Helsinki University of Technology, Espoo

Hämäläinen M and Ilmoniemi R 1994: Interpreting measured magnetic fields of the brain: minimum norm estimates *Med. & Biol. Eng. & Comput.* **32** 35–42

Hämäläinen M and Nenonen J 1999: Magnetic source imaging *Encyclopedia of Electrical Engineering Vol. 12* Ed. J Webster (New York: Wiley & Sons) 133–148

Johnston P and Gulrajani R 1997: A new method for regularization parameter determination in the inverse problem of electrocardiography *IEEE Trans. Biomed. Eng.* **44** 19–39

Kariniemi V, Ahopelto J, Karp P and Katila T 1974: The fetal magnetocardiogram *J. Perinat. Med.* **2** 214–216

Katila T and Karp P 1983: Magnetocardiography: morphology and multipole presentations *Biomagnetism, An interdisciplinary Approach* Eds. S Williamson *et al* (New York: Plenum Press) 237–263

Katila T, Maniewski R, Mäkijärvi M, Nenonen J and Siltanen P 1987: On the accuracy of source localisation in cardiac measurements *Phys. Med. Biol.* **32** 125–131

Katila T 1989: Principles and applications of SQUID sensors *Advances in Biomagnetism* Eds. S Williamson *et al* (New York: Plenum Press) 19–32

Khoury D S and Rudy Y 1992: A model study of volume conductor effects on endocardial and intracavitary potentials *Circ. Res.* **71** 511–525

Khoury D S, Taccardi B, Lux R L, Ershler P R and Rudy Y 1995: Reconstruction of endocardial potentials and activation sequences from intracavitary probe measurements. Localization of pacing sites and effects of myocardial structure *Circulation* **91** 845–863

Killmann R, Jaros G G, Wach P, Graumann R, Moshage W, Renhardt M and Fleischmann P H 1995: Localisation of myocardial ischaemia from the magnetocardiogram using current density reconstruction method: computer simulation study *Med. & Biol. Eng. & Comput.* **33** 643–651

Klepfer R, Johnson C and MacLeod R 1997: The effects of inhomogeneities and anisotropies on electrocardiographic fields: A 3–D finite–element study *IEEE Trans. Biomed. Eng.* **44** 706–719

Kobayashi K and Uchikawa Y 1999: Development of a three–dimensional biomagnetic measurement system with 39–channel SQUIDs *Recent Advances in Biomagnetism: Proceedings of the 11th International Conference on Biomagnetism* Eds. T Yoshimoto *et al* (Sendai: Tohoku University Press) 35–38

Lant J, Stroink G, ten Voorde B, Horáček B M and Montague T 1990: Complementary nature of electrocardiographic and magnetocardiographic data in patients with ischemic heart disease *J. Electrocardiol.* **23** 315–322

Leder U, Pohl H P, Michaelsen S, Fritschi T, Huck M, Eichhorn J, Müller S and Nowak H 1998: Noninvasive biomagnetic imaging in coronary artery disease based on individual current density maps of the heart *Int. J. Cardiol.* **64** 83–92

van Leeuwen P, Lange S, Bettermann H, Grönemeyer D and Hatzmann W 1999: Fetal heart rate variability and complexity in the course of pregnancy *Early Hum. Dev.* **54** 259–269

Liebman J, Zeno J, Olshansky B, Geha A, Thomas C, Rudy Y, Henthorn R, Cohen M and Waldo A 1991: Electrocardiographic body surface potential mapping in the Wolff–Parkinson–White syndrome: Noninvasive determination of the ventricular insertion sites of accessory atrioventricular connections *Circulation* **83** 886–901

Lindström M 1999: Characterization measurements of HT_C –SQUIDs *Diploma Thesis, Department of Engineering Physics and Mathematics, Helsinki University of Technology*

Liu Z W, Jia P, Biblo L A, Taccardi B and Rudy Y 1998: Endocardial potential mapping from a noncontact nonexpandable catheter: a feasibility study *Ann. Biomed. Eng.* **26** 994–1009

Lynn M and Timlake W 1968: The use of multiple deflations in the numerical solution of singular systems of equations, with applications to potential theory *SIAM J. Numer. Anal.* **5** 303–322

Lötjönen J, Reissman P–J, Magnin I, Nenonen J and Katila T 1998: A triangulation method of an arbitrary point set for biomagnetic problems *IEEE Trans. Magn.* **34** 2228–2233

Lötjönen J, Reissman P–J, Magnin I and Katila T 1999a: Model extraction from magnetic resonance volume data using the deformable pyramid *Medical Image Analysis* **3** 387–406

Lötjönen J, Magnin I, Reinhardt L, Nenonen J and Katila T 1999b: Reconstruction of 3–D geometry using 2–D profiles and a geometric prior model *IEEE Trans. Med. Imag.* **18** 992–1002

Lötjönen J 2000: Construction of boundary element models in bioelectromagnetism *Doctoral Thesis, Department of Engineering Physics and Mathematics, Helsinki University of Technology*

MacFarlane P W and Lawrie T D V 1988: *Comprehensive Electrocardiology* (Oxford: Pergamon Press)

MacLeod R S, Gardner M, Miller R M and Horáček B M 1995: Application of an electrocardiographic inverse solution to localize ischemia during coronary angioplasty *J. Cardiovasc. Electrophysiol.* **6** 2–18

Marquardt D 1963: An algorithm for least–squares estimation of nonlinear parameters *J. Soc. Indust. Appl. Math.* **11** 431–441

Martin R O, Pilkington T C and Morrow M N 1975: Statistically constrained inverse electrocardiography *IEEE Trans. Biomed. Eng.* **22** 487–492

Messinger–Rapport B and Rudy Y 1988: Regularization of the inverse problem of electrocardiography: A model study *Math. Biosci.* **89** 79–118

Montonen J 1995: MCG in identification of patients prone to malignant arrhythmias *Biomagnetism: Fundamental Research and Clinical Applications* Eds. C Baumgartner *et al* (Amsterdam: Elsevier Science/IOS Press) 606–611

Montonen J, Ahonen A, Hämäläinen M, Ilmoniemi R, Laine P, Nenonen J, Paavola M, Simelius K, Simola J and Katila T 2000: Magnetocardiographic functional imaging studies in BioMag Laboratory *Advances in Biomagnetism Research: Biomag96* Eds. C Aine *et al* (New York: Springer Verlag) in press

Morady F 1999: Radio–frequency ablation as treatment for cardiac arrhythmias *The New England Journal of Medicine* **340** 534–544

Morozov V 1984: *Methods for solving incorrectly posed problems* (New York: Springer Verlag)

Moshage W, Achenbach S, Weikl A, Göhl K, Bachmann K, Abraham Fuchs K, Härer W and Schneider S 1991: Clinical magnetocardiography: experience with a biomagnetic multichannel system *Int. J. Card. Imaging* **7** 217–223

Moshage W, Achenbach S, Göhl K and Bachmann K 1996: Evaluation of the non–invasive localization accuracy of cardiac arrhythmias attainable by multichannel magnetocardiography (MCG) *Int. J. Card. Imaging* **12** 47–59

Müller H P, Gödde P, Czerski K, Agrawal R, Feilcke G, Reither K, Wolf K J and Oeff M 1999: Localization of a ventricular tachycardia–focus with multichannel magnetocardiography and three–dimensional current density reconstruction *J. Med. Eng. Technol.* **23** 108–115

de Munck J 1992: A linear discretization of the volume conductor boundary integral equation using analytically integrated elements *IEEE Trans. Biomed. Eng.* **39** 986–990

Mäkijärvi M, Nenonen J, Leiniö M, Montonen J, Toivonen L, Nieminen M, Katila T and Siltanen P 1992: Localization of accessory pathways in Wolff–Parkinson–White syndrome by high–resolution magnetocardiographic mapping *J. Electocardiol.* **25** 143–155

Mäkijärvi M, Nenonen J, Toivonen L, Montonen J, Katila T and Siltanen P 1993: Magnetocardiography: supraventricular arrhythmias and preexcitation syndromes *Eur. Heart J.* **14** (Suppl. E) 46–52

Nenonen J, Purcell C J, Horáček B M, Stroink G and Katila T 1991a: Magnetocardiographic functional localization using a current dipole in a realistic torso *IEEE Trans. Biomed. Eng.* **38** 658–664

Nenonen J, Katila T, Leiniö M, Montonen J, Mäkijärvi M, and Siltanen P 1991b: Magnetocardiographic functional localization using current multipole models *IEEE Trans. Biomed. Eng.* **38** 648–657

Nenonen J, Mäkijärvi M, Toivonen L, Forsman K, Leiniö M, Montonen J, Järvinen A, Keto P, Hekali P and Katila T 1993: Non–invasive magnetocardiographic localization of ventricular pre–excitation in the Wolff–Parkinson–White syndrome using a realistic torso model *Eur. Heart J.* **14** 168–174

Nenonen J, Hämäläinen M and Ilmoniemi R 1994: Minimum–norm estimation in a boundary–element torso model *Med. & Biol. Eng. & Comput.* **32** 43–48

Nenonen J, Montonen J and Katila T 1996: Thermal noise in biomagnetic measurements *Rev. Sci. Instrum.* **67** 2397–2405

Netter F H 1991: *The CIBA collection of medical illustrations, Volume 5, the Heart* (Addison–Wesley, 7th edition)

Nowak H 1998: Biomagnetic instrumentation *Magnetism in Medicine* Eds. W Andrä and H Nowak (Berlin: Wiley–VCH) 88–135

Numminen J, Ahlfors S, Ilmoniemi R, Montonen J and Nenonen J 1995: Transformation of multichannel magnetocardiographic signals to standard grid form *IEEE Trans. Biomed. Eng.* **42** 72–78

Oeff M and Burghoff M 1994: Magnetocardiographic localization of the origin of ventricular ectopic beats *Pacing Clin. Electrophysiol.* **17** 517–522

Oostendorp T F and van Oosterom A 1991: Modelling the fetal magnetocardiogram *Clin. Phys. Physiol. Meas.* **12** (Suppl. A) 15–18

Oostendorp T F, Nenonen J and Huiskamp G 1996: Comparison of inverse solutions obtained from ECG and MCG data *Proc IEEE–EMBS Conf* (CD–ROM)

Oostendorp T, MacLeod R and van Oosterom A 1997: Non–invasive determination of the activation sequence of the heart: validation with invasive data *Proc IEEE–EMBS Conf* (CD–ROM) 335–338

van Oosterom A and Strackee J 1983: The solid angle of a plane triangle *IEEE Trans. Biomed. Eng.* **30** 125–126

van Oosterom A, Oostendorp T F, Huiskamp G and ter Brake H J 1990: The magnetocardiogram as derived from electrocardiographic data *Circ. Res.* **67** 1503–1509

van Oosterom A 1999: The use of the spatial covariance in computing pericardial potentials *IEEE Trans. Biomed. Eng.* **46** 778–787

Oster H S and Rudy Y 1992: The use of temporal information in the regularization of the inverse problem of electrocardiography *IEEE Trans. Biomed. Eng.* **39** 65–75

Oster H S and Rudy Y 1997: Regional regularization of the electrocardiographic inverse problem: a model study using spherical geometry *IEEE Trans. Biomed. Eng.* **44** 188–199

Oster H S, Taccardi B, Lux R L, Ershler P R and Rudy Y 1997: Noninvasive electrocardiographic imaging: reconstruction of epicardial potentials, electrograms, and isochrones and localization of single and multiple electrocardiac events *Circulation* **96** 1012–1024

Paavola M, Ilmoniemi R, Sohlström L, Meinander T, Penttinen A and Katila T 2000: High performance magnetically shielded room for clinical measurements *Advances in Biomagnetism Research: Biomag96* Eds. C Aine *et al* (New York: Springer Verlag) in press

Plonsey R 1969: *Bioelectric Phenomena* (New York: McGraw–Hill)

Plonsey R 1972: Capability and limitations of electrocardiography and magnetocardiography *IEEE Trans. Biomed. Eng.* **19** 239–244

Press W H, Teukolsky S A, Vetterling W T and Flannery B P 1993: *Numerical Recipes in C : The Art of Scientific Computing (2nd edition)* (Cambridge University Press)

Purcell C J, Stroink G, Horáček B M 1988: Effect of torso boundaries on electric potential and magnetic field of a dipole *IEEE Trans. Biomed. Eng.* **35** 671–678

Purcell C J and Stroink G 1991: Moving dipole inverse solutions using realistic torso models *IEEE Trans. Biomed. Eng.* **38** 82–84

Ribeiro P C, Bruno A C, Saboia e Silva P L, Barbosa C R, Ribeiro E P, Monteiro E C and Costa A F 1992: Detection of reentry currents in atrial flutter by magnetocardiography *IEEE Trans. Biomed. Eng.* **39** 818–824

Roth B J and Wikswo J P Jr. 1986: Electrically silent magnetic fields *Biophys. J.* **50** 739–45

Rudy Y and Messinger–Rapport B 1988: The inverse problem in electrocardiography: solutions in terms of epicardial potentials *Crit. Rev. Biomed. Eng.* **16** 215–268

Savard P, Roberge F A, Perry J B and Nadeau R A 1980: Representation of cardiac electrical activity by a moving dipole for normal and ectopic beats in the intact dog *Circ. Res.* **46** 415–425

Savard P, Mailloux G E, Roberge F A, Gulrajani R M and Guardo R 1982: A simulation study of the single moving dipole representation of cardiac activity *IEEE Trans. Biomed. Eng.* **29** 700–707

Savard P, Cohen D, Lepeschkin E, Cuffin B N and Madias J E 1983: Magnetic measurement of S–T and T–Q segment shifts in humans. Part I: Early repolarization and left bundle branch block *Circ. Res.* **53** 264–273

Savard P, Ackaoui A, Gulrajani R M, Nadeau R A, Roberge F A, Guardo R and Dube B 1985: Localization of cardiac ectopic activity in man by a single moving dipole, comparison of different computation techniques *J. Electrocardiol.* **18** 211–222

Scholz B and Schwierz G 1994: Probability–based current dipole localization from biomagnetic fields *IEEE Trans. Biomed. Eng.* **41** 735–742

Sekihara K and Scholz B 1996: Generalized Wiener estimation of three–dimensional current distribution from biomagnetic measurements *IEEE Trans. Biomed. Eng.* **43** 281–291

Shahidi A, Savard P and Nadeau R 1994: Forward and inverse problem in electrocardiography: modeling and recovery of epicardial potentials in humans *IEEE Trans. Biomed. Eng.* **41** 249–256

Shaw R M and Rudy Y 1997a: Electrophysiologic effects of acute myocardial ischemia. A mechanistic investigation of action potential conduction and conduction failure *Circ. Res.* **80** 124–138

Shaw R M and Rudy Y 1997b: Electrophysiologic effects of acute myocardial ischemia: a theoretical study of altered cell excitability and action potential duration *Cardiovasc. Res.* **35** 256–272

Siltanen P 1988: Magnetocardiography *Comprehensive Electrocardiology* Eds. P W MacFarlane and T D V Lawrie (Oxford: Pergamon Press) Ch. 38

Simelius K, Tierala I, Jokiniemi T, Nenonen J, Toivonen L and Katila T 1996: A body surface potential mapping system in clinical use *Med. Biol. Eng. Comput.* **34** (Suppl. 1, Pt 2) 107–108

Simelius K 1998: Development of cardiographic mapping techniques for clinical use *Licentiate Thesis, Department of Engineering Physics and Mathematics, Helsinki University of Technology*

SippensGroenewegen A, Spekhorst H, van Hemel N, Kingma J, Hauer R, de Bakker J, Grimbergen C, Janse M and Dunning A 1993: Localization of the site of origin of postinfarction ventricular tachycardia by endocardial pace mapping *Circulation* **88** 2290–2306

Stroink G, Lamothe R and Gardner M J 1996: Magnetocardiographic and electrocardiographic mapping studies *SQUID Sensors: Fundamentals, Fabrication and Applications* Ed. H Weinstock (Kluwer: NATO ASI Series) 413–444

Takala P 1999: Magnetocardiography in exercise studies and in the detection of left ventricular hypertrophy *Licentiate Thesis, Department of Engineering Physics and Mathematics, Helsinki University of Technology*

Takala P, Montonen J, Aalto T, Mäkijärvi M, Nenonen J, Yildirim Y, Nieminen M and Katila T 2000: Magnetocardiographic assessment of left ventricular hypertrophy: Correlation with echocardiography *Advances in Biomagnetism Research: Biomag96* Eds. C Aine *et al* (New York: Springer Verlag) in press

Tan G A, Brauer F, Stroink G and Purcell C J 1992: The effect of measurement conditions on MCG inverse solutions *IEEE Trans. Biomed. Eng.* **39** 921–927

Tenner U, Haueisen J, Nowak H, Leder U and Brauer H 1999: Source localization in an inhomogeneous physical thorax phantom *Phys. Med. Biol.* **44** 1969–1981

Thivierge M, Gulrajani R M and Savard P 1997: Effects of rotational myocardial anisotropy in forward potential computations with equivalent heart dipoles *Ann. Biomed. Eng.* **25** 477–498

Tikhonov A N and Arsenin V Y 1977: *Solutions of Ill–Posed Problems* (Washington DC: Winston & Sons)

Tilg B, Wach P, Rucker W and Kynor D 1995: Biomagnetic functional localisation: iterative approach to estimation of electrical sources within the human heart from the magnetocardiogram *Med. Biol. Eng. Comput.* **33** 238–240

Tilg B, Nenonen J, Lafer G, Fischer G, Wach P and Katila T 1997: A comparison study on source imaging from BSP and MCG data *Biomedizinische Technik* **42** (Suppl. 1) 151–154

Tilg B, Modre R, Fischer G, SippensGroenewegen A, Mlynash M, Roithinger F X, Reddy G, Roberts T, Wach P, Lesh M D and Steiner P R 1999: Validation of noninvasive functional cardiac electrical source in a 43–year old male patient *Biomedizinische Technik* **44** (Suppl. 2) 147–151

Tripp J H 1983: Physical concepts and mathematical models *Biomagnetism, An interdisciplinary Approach* Eds. S Williamson *et al* (New York: Plenum Press) 101–139

Uutela K, Hämäläinen M and Salmelin R 1998: Global optimization in the localization of neuromagnetic sources *IEEE Trans. Biomed. Eng.* **45** 716–723

Virtanen J, Parkkonen L, Ilmoniemi R, Pekkonen E and Näätänen R 1997: Biopotential amplifier for simultaneous operation with biomagnetic instruments *Med. Biol. Eng. Comput.* **35** 402–408

Wach P, Tilg B, Lafer G and Rucker W 1997: Magnetic source imaging in the human heart: estimating cardiac electrical sources from simulated and measured magnetocardiogram data *Med. Biol. Eng. Comput.* **35** 157–166

Wakai R T, Leuthold A C, Wilson A D and Martin C B 1997: Association of fetal junctional rhythm and respiratory arrhythmia detected by magnetocardiography *Pediatr. Cardiol.* **18** 201–203

Wei D, Okazi O, Harumi K, Harasawa E and Hosaka H 1995: Comparative simulation of excitation and body surface electrocardiogram with isotropic and anisotropic computer models *IEEE Trans. Biomed. Eng.* **42** 343–357

Weismüller P, Abraham Fuchs K, Schneider S, Richter P, Kochs M and Hombach V 1992: Magnetocardiographic non–invasive localization of accessory pathways in the Wolff–Parkinson–White syndrome by a multichannel system *Eur. Heart J.* **13** 616–622

Yamashita Y and Geselowitz D 1985: Source–field relationships for cardiac generators on the heart surface based on their transfer coefficients *IEEE Trans. Biomed. Eng.* **32** 964–970